

Electrical control of hot carrier transfer in WS₂/Graphene heterostructures

Master thesis
(M.Sc. in Nanoscience and Nanotechnology)

Submitted by
Aliaa Sayed Hassan Mohamed
1383926

University of Siegen
Faculty of Science and Technology
Department Chemistry-Biology
01.12.2020

Under the supervision of Dr. Hai Wang
Prof. Mischa Bonn
Prof. Thomas Lenzer

The work described in this master thesis was performed in the Molecular spectroscopy department (Nano-optoelectronic group) at the Max Planck Institute for Polymer Research.

Table of Contents

Abstract	5
1. Motivation and literature	6
1.1. Motivation	6
1.2.1. Charge carrier dynamics in graphene	8
1.2.2. Charge carrier dynamics in WS ₂ /Gr heterostructures.....	11
1.2.2.1. Interfacial charge transfer and recombination process at the interface of WS ₂ /Gr heterostructure (in sub A-exciton excitation regime)	14
1.2.2.2. Interfacial charge transfer process at the interface of WS ₂ /Gr heterostructure (in above A-exciton excitation regime)	16
2. Terahertz spectroscopy	18
2.1. Terahertz radiation.....	19
2.2. Terahertz setup	19
2.3. Measurement techniques.....	21
2.3.1. THz time-domain spectroscopy (THz-TDS).....	21
2.3.2. Optical-pump THz-probe spectroscopy (OPTP)	23
2.4. Theory	23
2.4.1. THz generation	23
2.4.2. THz detection by electro-optic sampling.....	26
2.5. Calculation of complex parameters from THz measurements	28
2.6. Conductivity models.....	30
2.6.1. Drude model	30
2.6.2. Drude-Smith model.....	31
2.6.3. Lorentz oscillator model.....	32
3. Experiments and results	33
3.1. Device fabrication and characterization.....	33
3.2. In situ electrical and OPTP measurements	35
3.3. Discussions and results.....	36
Discussion 1: The interfacial charge transfer process at varied graphene Fermi levels.....	36

Discussion 2: The interfacial charge recombination dynamics at varied graphene Fermi levels	39
3.4. Conclusion	43
3.5. Supporting information	44
Section 1: Fabrication methods	44
Section 2: Theoretical calculation	46
References	49

Abstract

Van der Waals (vdW) heterostructures consisting of graphene (Gr) and transition metal dichalcogenides (TMDs) have recently emerged as a novel platform for highly efficient photodetectors. The device performance critically relies on charge transfer (CT) dynamics across the interfaces. However, the underlying mechanism for interfacial charge carrier dynamics remains highly debated. Employing Terahertz spectroscopy, this thesis aims to provide a comprehensive understanding of the hot carrier transfer (HCT) and charge carrier recombination processes at WS_2/Gr interface by tuning the Fermi level of graphene via ionic gating. By only exciting graphene in the heterostructure (using laser pulses of 800 nm, energy below the bandgap of monolayer WS_2), we observed injection of hot electrons from graphene to WS_2 , in line with previous reports. More importantly, by studying the dependence of HCT efficiency on different Fermi levels in graphene, we show that, following optical excitations, injection of thermalized hot electrons, rather than that of injection of non-thermalized hot electrons, governs the HCT processes. Secondly, the gating dependent recombination dynamics reveals a critical role of the defect states on the photogating effect. Our results suggest that the defect states in the heterostructure can be electrochemically controlled (occupied or unoccupied) and have a substantial impact on the photogating processes. For the heterostructure with p-doped graphene, these defect states are unoccupied and can effectively capture the injected hot electrons from the conduction band of WS_2 , leading to a photogating effect by the trapped electrons. On the other hand, for the heterostructure with n-doped graphene, where the defects are supposed to be filled electrochemically, we reported a switching in the photogating mechanism: we show that holes trapped in the defects are responsible for the long-lived photogating effect. These results provide new insights on both HCT and recombination processes in TMDs/Gr heterostructures with potential applications in photodetection.

1. Motivation and literature

1.1. Motivation

Graphene and transition metal dichalcogenides (TMDs) are atomically thin building blocks that are emerged recently for high-performance low-dimensional optoelectronic devices. These 2D materials can form Van der Waals (vdW) heterostructures by stacking the exfoliated individual layers. The formed vdW heterostructures offer potentially new optical, electronic, and magnetic properties excelling their bulk counterparts [1]-[4]. In the last decade, numerous functional devices based on vdW heterostructures have emerged, thanks to the easiness in tuning the layer number, coupling strength, compositions, stacking angle, and sequence of the atomic layers [5]-[7]. WS₂/graphene (WS₂/Gr) heterostructure, as a promising combination, is the focus of this study as photodetectors based on this configuration shows an ultrahigh photoresponsivity ($\sim 10^6$ AW⁻¹) at room temperature compared to other materials, as shown in figure (1.1) [8]. To achieve an ultrahigh photoresponsivity (R) in the photodetectors, a long interfacial charge separation lifetime (t_1) is required according to the following equation [8]:

$$R = \frac{I_{\text{photon}}}{P_{\text{inc}}} = \frac{\eta \theta t_1}{h\nu t_2} \quad (1.1)$$

where t_2 , $h\nu$ and η are carrier transient time, photon energy, and quantum efficiency of the interfacial charge transfer (CT), respectively.

To increase R , a high interfacial CT quantum yield η and further a long-lived charge separation time t_1 are required. However, for both CT and recombination processes, the detailed mechanisms remain elusive and debated. Besides, little work has been done to achieve tuning of the CT and recombination process (including efficiency and lifetime). In this thesis, the aim is to understand and tune the CT and recombination dynamics by electrochemically controlling the Fermi level in graphene. To simply the experimental condition, here we focus on an excitation regime, in which only the graphene is excited. More precisely, we attempt to address the following two questions:

- (1) For CT: previous studies have shown that following photoexcitation, hot electrons in graphene can be injected into the WS₂ layer [9]. However, it remains debated if hot-electron transfer (HET) from graphene to WS₂ takes place before or after thermalization in graphene. The HET efficiency dependence on Fermi levels in graphene is a critical parameter to differentiate these two pathways: tuning the Fermi level in graphene will lead to a substantial change in the CT efficiency for injection of thermalized hot electrons. This is because both electron temperature

and energy barriers, two critical parameters for thermalized HET, are modulated with changes in Fermi level. On the other hand, injection of non-thermalized, nascent hot electrons will not be strongly influenced by the Fermi level in graphene within the Fermi level ranges achieved in the study. Therefore, to answer this question, it is important to study how the tuning of the Fermi level in graphene affects the interfacial CT process.

- (2) For charge separation lifetime t_1 : combined THz and transient absorption (TA) spectroscopies, Fu et.al [9] has recently reported a long-lived charge separation in WS_2/Gr heterostructures, in line with an ultrahigh photoresponsivity previously reported for the WS_2/Gr photodetectors. The long t_1 in the WS_2/Gr heterostructure is achieved by photogating mechanism: following photoexcitation and interfacial CT, the electrons that are injected into the WS_2 conduction band can be rapidly (~ 1 ps) trapped by the unoccupied defect states in WS_2 . A charge recombination bottleneck from the localized defect states in WS_2 to graphene results in a long-lived (over ns) photoconductive gain in WS_2 for efficient photodetection [9]. Following up this study, it is critical to further address the impact of nature (occupied or unoccupied) and density of defects on the photogating effect in WS_2/Gr heterostructures, by tuning the Fermi level in graphene.

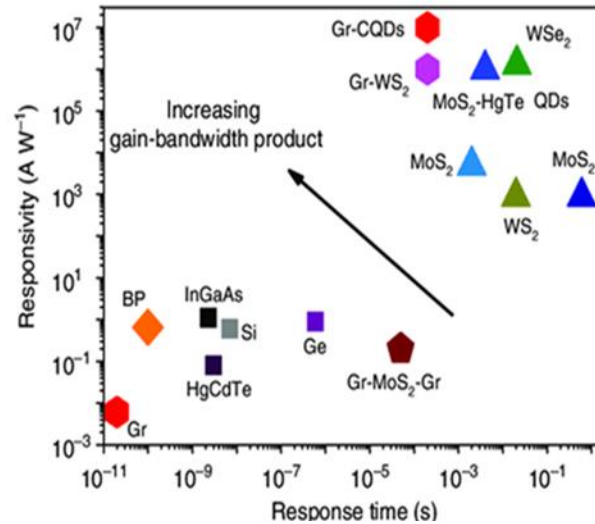


Figure 1.1: Recent development in the performance of photodetectors based on low dimensional materials [8].

1.2. Literature

1.2.1. Charge carrier dynamics in graphene

Graphene is a single layer of carbon atoms with a honeycomb lattice. It has a linear electronic band structure where the charge carriers are endowed with high mobility at room temperature and behave as 2D massless Dirac Fermions [10]-[15]. Graphene exhibits a broadband optical absorption (2.3%) ranging from far-infrared to visible range. The optical absorption of graphene in the IR-vis region is due to the interband transition (the optical conductivity is close to the universal value $\sigma_0 = \pi e^2/2h$). However, in the low-frequency region (e.g. THz), the optical absorption is due to intraband transition (that varies with the charge density) [14]-[16]. The carrier density of graphene can be controlled by tuning its Fermi level either by electrostatic gating or chemical doping [17]. The combination of unusual electrical and optical properties of graphene makes it a good candidate for THz optoelectronic, photo-sensing, photovoltaic, and plasmonic applications [17]-[19]. Recently, many efforts have been focused on understanding charge carrier dynamics in graphene for developing next-generation broadband photodetectors, hot-carrier transistors [20], and solar cells [21]. The transient optical response of graphene following photoexcitation can be studied by a pump-probe technique such as optical-pump THz-probe spectroscopy (OPTP). In this technique, an optical pulse excites the sample and single-cycle THz pulses (with ~ 1 ps duration) probe the pump-induced conductivity change as a function of pump-probe delay. Upon the optical excitation of the graphene, the electrons and holes are generated immediately. The generated hot carriers have definite temperature T_e after thermalization, forming a well-defined Fermi Dirac distribution around the initial Fermi energy [22]. The OPTP provides information about the evolution of the Fermi Dirac distribution during the heating and cooling of hot carriers in graphene [23]. The OPTP was used before to study the transient conductivity in different graphene samples (exfoliated, epitaxial, or chemical vapor deposition “CVD”) [24]-[29] and in different gas species [29]. It has been found that the sign of transient THz conductivity differs in different graphene samples. For instance, the epitaxial multilayered graphene on SiC substrate exhibits a positive transient THz conductivity (a decrease in THz transmission and thus faster cooling process) [27], [28]. However, the single-layer CVD graphene exhibits negative THz photoconductivity (an increase in THz transmission and thus slower cooling process) [24]-[26]. The opposite behaviors arise from the difference in the initial Fermi level in different samples [14]. The increase of THz transmission observed in CVD graphene is because that CVD graphene is always unintentionally highly-doped and behaves like a semimetal. Graphene exhibits different photoinduced THz response at different doping levels, switching from

semiconducting behavior (with positive THz photoconductivity near the charge neutral point) to metallic behavior (with negative THz photoconductivity in a highly doped regime). Such a transition is a unique property for zero-bandgap materials such as graphene [23]. Despite the change in the sign of photoinduced THz conductivity, the decay dynamics of the THz conductivity remain similar at different Fermi levels [23], [24], [28]. The transient THz conductivity of the single-layer CVD graphene on a fused SiO₂ substrate can be measured via THz time-domain spectroscopy [30]. The difference in frequency-dependent THz transmission ($\Delta E(\omega) = E(\omega) - E_0(\omega)$) between the bare fused SiO₂ substrate $E_0(\omega)$ and graphene on fused SiO₂ substrate $E(\omega)$ is proportional to the frequency-resolved conductivity of graphene $\Delta\sigma(\omega)$ following this equation:

$$\Delta\sigma(\omega) \approx -\left(\frac{n_s+1}{Z_0}\right) \frac{\Delta E(\omega)}{E_0(\omega)} \quad (1.2)$$

where Z_0 is the vacuum impedance (337 Ω), n_s is the refractive index of the substrate (in the case of the fused silica in the range of 0.3-1 THz, $n=1.96$) [30]. It has been found that the conductivity of graphene is determined by Drude weight D and scattering rate Γ , and can be written as: [14], [23].

$$\sigma \approx \frac{D}{\Gamma} \quad (1.3)$$

Upon photoexcitation, the photo-induced change in conductivity (i.e. photoconductivity) becomes:

$$\Delta\sigma \approx \left(\frac{\Delta D}{D_0} - \frac{\Delta\Gamma}{\Gamma_0}\right) \quad (1.4)$$

where

$$\Delta D = G_0 \times 2k\Delta T_e \ln 2$$

D_0 and Γ_0 are the Drude weight and the scattering rate without pump, respectively, and ΔD and $\Delta\Gamma$ are the pump-induced change in Drude weight and scattering rate, respectively. The contribution from the Drude weight and scattering rate to the Drude conductivity varies at different Fermi energy levels [14], [23]. In the charge neutral point graphene, the photoconductivity is dominated by the change in Drude weight, because the photoexcitation increases the net conducting carrier density following this equation:

$$\Delta n = \frac{\pi}{3} \left(\frac{KT_e}{\hbar v_F}\right)^2 \quad (1.5)$$

However, in highly-doped graphene, the photoconductivity is dominated by the change in scattering rate due to the increase of the scattering events [17], [25]. It is confirmed experimentally [17], [31] and theoretically [17] that the negative photoconductivity in highly-doped graphene arises from the high electronic temperature. The high electronic temperature leads to the redistribution of electrons and holes in the conduction and valence band, shifting the effective Fermi energy level (quasi-equilibrium) according to the following equation [32]:

$$\Delta|E_F| \approx -\frac{\pi^2}{6} \left(\frac{K_B T_e}{E_2} \right)^2 \quad (1.6)$$

The intraband transition in graphene depends on the charge density. Graphene exhibits a distinctive nonmonotonic temperature dependence on the intraband absorption strength or Drude weight due to its linear energy dispersion [14], [32], [33]. In contrast, the materials with massive particles and parabolic energy dispersion show temperature independence on the Drude weight [14], [32], [33].

The photoconductivity of graphene shows a sublinear dependence on the pump fluence. The dependence changes from $P^{1/3}$ in the charge-neutral point graphene [23] to $P^{1/2}$ in highly-doped graphene [23], [24], [36], [38]. The distinct power law can be explained by the heat capacities C_e as a function of Fermi levels via:

$$C_e = \alpha T_e \quad (1.7)$$

where

$$\alpha = \left[\frac{2\pi E_F}{3\hbar^2 v_F^2} \right] K_B^2$$

where \hbar , v_F and K_B are the reduced Planck constant, Fermi velocity, and Boltzmann's constant, respectively [9], [23], [33]. At the charge neutral point, graphene has a low heat capacity. This means the photoexcitation heats the electrons efficiently, leading to more intraband carrier-carrier scattering cascade events to relax, ending up with efficient carrier multiplication [17], [23]. Above a certain high fluence and carrier temperature (~ 4000 K), the photoconductivity shows a saturation behavior.

Upon photoexcitation, hot carriers in graphene exhibit two relaxation pathways for carrier heating: carrier-carrier scattering and phonon emission [17]. The THz spectroscopy can investigate the dominated energy relaxation pathway in the ultrafast energy relaxation (on the sub-ps level), and the branching ratios between the competing pathways are affected by the Fermi energy level and pump fluence [17]. At low fluences (also at higher Fermi energies), where a large amount of absorbed photon

energy is transferred to the electronic system, the relaxation process is dominated by the efficient carrier-carrier scattering. Therefore, the carrier heating (the fraction of the absorbed and transferred energy from the incident light to the electronic system) is sufficiently high, close to 100%. In contrast, at high fluences (also at low Fermi energies), the carrier-carrier scattering events cannot transfer the energy very efficiently. Therefore, a large fraction of absorbed energy is transferred to the lattice by phonon emission, decreasing the carrier heating efficiency [17]. In conclusion, in slightly-doped graphene (or undoped graphene), the phonon emission pathway dominates the ultrafast energy relaxation and leads to carrier multiplication (multiplication of excitation of electrons and holes) due to the interband transition [39]-[41]. However, in highly-doped graphene, carrier-carrier scattering dominates the ultrafast energy relaxation. The efficient carrier-carrier scattering increases the carrier temperature due to intraband transition and hence the carrier heating efficiency increases [42]-[44]. In other words, the efficient carrier heating in highly-doped graphene attributes to its negative photoconductivity [11], [24], [31].

The unique ability to tune the ultrafast relaxation energy and carrier heating in graphene gives it credits to be implemented in advanced photodetectors, where the hot carriers play a critical role in the photocurrent generation [17], [21].

1.2.2. Charge carrier dynamics in WS₂/Gr heterostructures

In principle, as discussed in section 1.2.1, following photoexcitation of monolayer graphene, the generated non-thermalized carriers can transfer their excess energy to the other carriers via carrier-carrier, carrier-phonon scatterings. The hot carriers then end up being thermalized with a well-defined electronic temperature T_e following Fermi Dirac distribution (within ~tens of fs). The thermalized hot carriers then cool down by transferring their excess energy to the lattice and substrate via carrier-phonon scattering on the ps level [10]-[19]. To harvest the energy of these hot carriers, an ultrafast transport channel is needed to capture these hot carriers before they dissipate their excess energy to the environment [20].

2D vdW heterostructures consisting of graphene and TMDs layers, in particular, the WS₂/Gr system, represent a novel platform for harvesting hot electrons in graphene for optoelectronic devices due to strong interlayer electronic coupling [43]. Ultrafast spectroscopy studies confirmed that the hot carrier transfer contributes to the photocurrent generation at the interface of the WS₂/Gr heterostructure [10], [44], [45]. The hot carrier transfer mechanism differs depending on the excitation energy. For example, when WS₂/Gr is photoexcited above WS₂ A-exciton (> 2 eV), both the graphene and WS₂ are excited as shown in figure (1.2b) [9], [43]. In this regime, direct hole transfer dominates the charge transfer pathway, and the holes transfer from the

WS₂ valence band to the valence band of graphene with an efficiency ~5% [9]. However, when the WS₂/Gr is photoexcited below the A-exciton of the WS₂ (< 2 eV), only the graphene is excited as shown in figure (1.2a). There are many debates about the charge transfer pathway, e.g. whether it takes place before or after the thermalization process [10], [44], [45]. A recent study has supposed that the sub-A exciton excitation of the WS₂/Gr heterostructure, leads to a photocurrent generation via photo-thermionic emission (PTE, the charge transfer occurs after the thermalization process) [9]. This is in good agreement with the charge transfer pathway observed in Gr-WSe₂-Gr with excitations below the bandgap of WSe₂. Through the photo-thermionic emission “hot carrier injection” mechanism, the incident photon with an energy of E_{photon} is absorbed by the graphene layer, creating photoexcited carriers in graphene with an energy of $E = \frac{E_{photon}}{2}$. The carriers interact with each other via carrier-carrier scattering, forming a quasi-equilibrium distribution with an elevated electron temperature. Only the hot thermalized carriers with sufficient energy to overcome the Schottky barrier can be injected from graphene to WS₂ layer [9], [44], [45], [47]. The hot electron injection mechanism in figure (1.3a) is found to be inefficient (~1%) [46]. On the other hand, one recent study has reported a highly efficient (~50%) pathway called a direct hot-electron transfer (or non-photo-thermionic pathway, non-PTE), where the nascent hot-carrier transfer competes with the thermalization process in WS₂/Gr heterostructure [10] as shown in figure (1.3b).

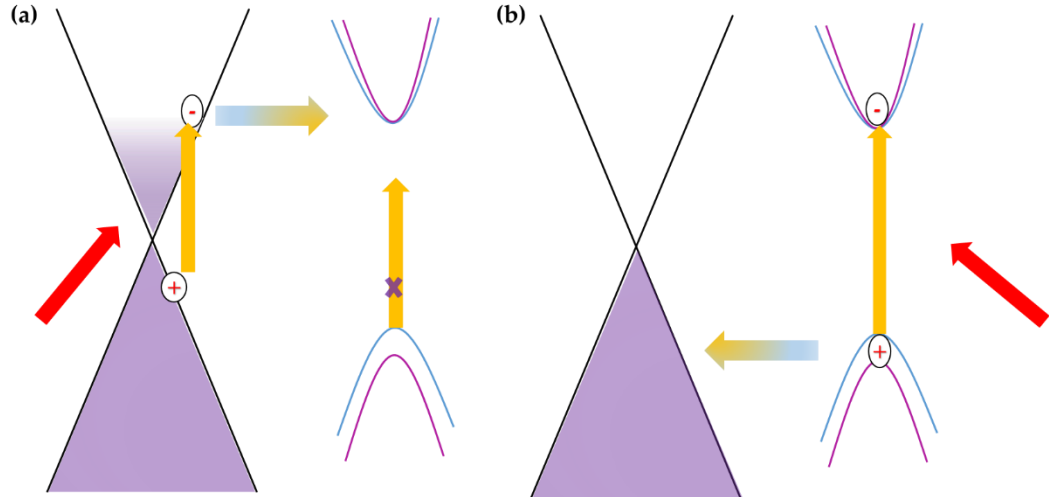


Figure 1.2: (a) Graphene excitation below the sub-A exciton of TMDs, where photo-thermionic emission dominated the charge transfer pathway with ~ 1% efficiency, (b) TMDs excitation above A-exciton resonance, where direct hole transfer dominates the charge transfer pathway with ~ 5% efficiency.

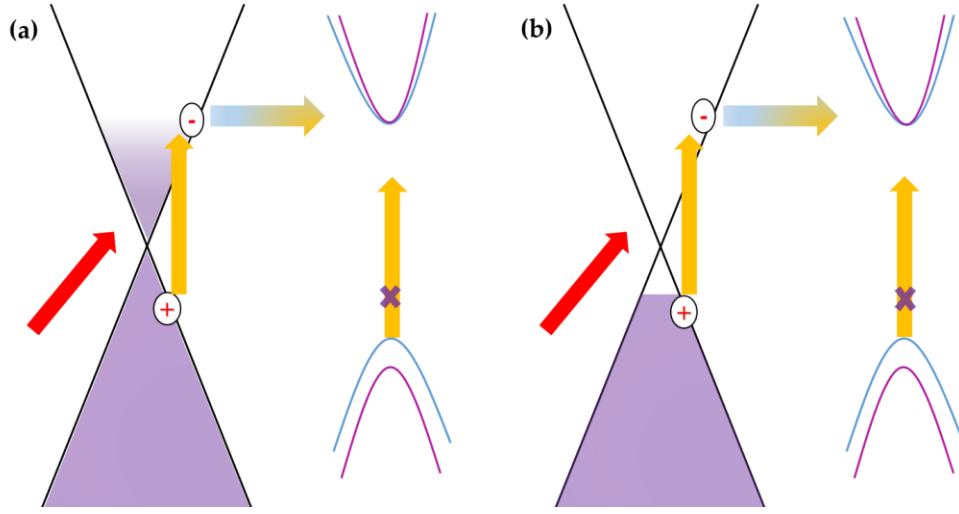


Figure 1.3: (a) Photo-thermionic emission pathway, where the charge transfer occurs after the thermalization process, (b) direct hot-electron transfer pathway, where the charge transfer competes with the thermalization process across WS₂/Gr interfaces

The photoconductivity dependence on pump fluence is an effective parameter to distinguish the charge transfer mechanisms (either PTE and direct hot-electron transfer pathways in sub-A exciton excitation or direct hole transfer above A-exciton excitation) and their efficiency [9], [10], [43], [44]. It is observed that the WS₂/Gr heterostructure undergoes the photo-thermionic pathway, exhibits a photocurrent generation (maximum positive photoconductivity) that has a superlinear dependence on the pump fluence P^α , where the power index $\alpha > 1$. The photo-thermionic pathway depends on the electron temperature that relies on the incident fluence [46]. However, the non-photo-thermionic charge transfer pathway exhibits a linear pump fluence dependence P^α ($\alpha = 1$) [44]. In the photoexcitation above the A-exciton (> 2 eV), direct hole transfer takes place in which the photogenerated holes in the valence band of WS₂ can transfer to the valence band of graphene with an efficiency of ~5% however, the photogenerated electrons in WS₂ are trapped [9]. This mechanism shows a slightly sublinear pump fluence ($\alpha < 1$) dependence because of many-body effects (exciton-exciton annihilation in WS₂) start to play a role at high fluences [9].

As mentioned before the ultrahigh photoresponsivity in photodetectors requires a long charge separation lifetime according to equation (1.1). There are many contrary observations and debates about the charge separation lifetime at WS₂/Gr interface. For instance, a charge separation lifetime (~ 1 ps) is suggested by TA spectroscopy, based

on an observation of ultrafast electron depopulation dynamics from the excited states of WS₂ following its population process via HET from graphene to WS₂. On the other hand, a long-lived charge separation lifetime (~ 1 ns) has been proposed by using THz spectroscopy which tracks the carrier dynamics in graphene [9]. Based on these results, Fu et.al provides a photogating scenario, in which the injected electrons occupied the A-exciton state shortly, and subsequently captured by unoccupied defects in WS₂ in ~ 1 ps (probed by TA) [9]. Due to the localized nature of these defects, the trapped electrons experienced a recombination bottleneck with holes in graphene. This leads to a long-lived conductivity modulation observed by THz [9].

1.2.2.1. Interfacial charge transfer and recombination process at the interface of WS₂/Gr heterostructure (in sub A-exciton excitation regime)

First, let us discuss the interplay between the interfacial charge transfer dynamics and the ultrahigh photoresponsivity in WS₂/Gr based photodetectors. When a bare monolayer WS₂ is photoexcited below its A-exciton, it exhibits no photobleaching signals in TA spectra [9]. In other words, no charge occupation takes place in the WS₂ excited state and hence shows no photoconductivity as shown in figure (1.4a, blue line) [9], [10], [43], [45]. For a bare monolayer CVD graphene, following photoexcitation at the same pump energy (below A-exciton of WS₂), it shows a transient reduction in photoconductivity as observed in figure (1.4a, grey line) in agreement with previous studies [9], [10], [14], [17], [23]-[25], [27], [33], [50], [51], due to carrier heating effect discussed in the last sections. When the WS₂/Gr heterostructure is photoexcited below the A-exciton resonance of WS₂, two photobleaching signals are observed in TA spectra at ~ 2 and ~ 2.4 eV, corresponding to A- and B-exciton resonances of the WS₂ monolayer, which only appear in the heterostructure as shown in figure (1.4b). The simultaneous occurrence photobleaching of both A- and B-exciton resonances proves the injection of hot electrons rather than hot holes from graphene to WS₂ at the interface [9]. This observation is further confirmed via THz spectroscopy [9], where the transient photoconductivity response of the heterostructure is not the superposition of transient responses of WS₂ and graphene. However, it exhibits short-lived negative photoconductivity (with sub-10 ps lifetime) followed by long-lived positive photoconductivity (with ~ 1 ns lifetime) as shown in figure (1.4a) (red line) [9]. The short-lived negative photoconductivity corresponds to the intrinsic hot carrier state in the graphene [9], [10], [14], [17], [23]-[25], [27], [33], [50], [51]. However, the long-lived positive photoconductivity which appears only in the heterostructure is due to the

interfacial charge transfer, and subsequently, a photogating effect that is mediated by the interfacial states at WS₂/Gr interface [9].

The energy barrier for the charge carrier transfer between WS₂ conduction band minimum and Fermi level of graphene is 0.8 eV, taking into account the dielectric screening from graphene that leads to bandgap reduction in WS₂ [49] and shift in the energies due to the charge transfer process [9]. The interfacial states originate either from the hybridized states at the interface or the defect states from the sulfur vacancies in the CVD WS₂. The interfacial states from the sulfur vacancies lie at ~0.5 and ~0.7 eV below the conduction band of WS₂ [9], [50]. Since these empty states lie between the Fermi level of graphene and the conduction band of WS₂, the (thermalized and non-thermalized) hot carriers involve in the interfacial charge transfer process at WS₂/Gr interface. Therefore, the interfacial states act as intermediate trapping states [9], where the photogenerated electrons in graphene transfer to the WS₂ conduction band on sub-ps and then get trapped for ~1 ns [9]. This long-lived charge separation at the interface can effectively gate graphene (photogating effect) by establishing an electric field at the interface and hence graphene's carrier density and Fermi level will be tuned. The positive photoconductivity offset is observed because, upon photoexcitation of initially highly-doped graphene, the electrons are injected from graphene to WS₂ conduction band within < 150 fs [9], shifting the Fermi level down away from the Dirac point [43] (the shift of the Fermi level can be confirmed by THz-TDS, section 3 in chapter 2) [9]. By increasing the absorbed photon density (via increasing fluence), the long-lived positive photoconductivity increases [9]. This photogating mechanism causes a photoconductive gain that leads to the ultrahigh photoresponsivity in WS₂/Gr based photodetectors.

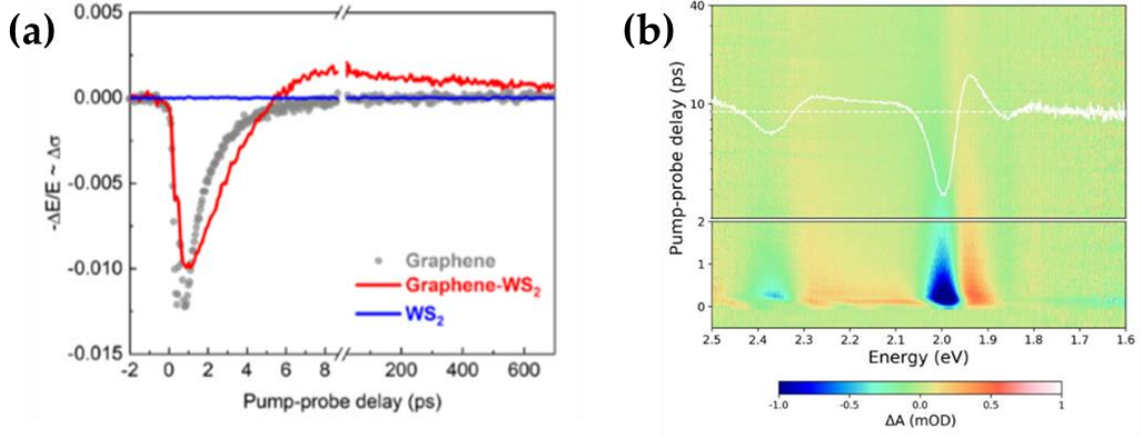


Figure 1.4: (a) Photoconductivity of monolayer layer WS₂, monolayer graphene, and the WS₂/Gr heterostructure following 1.55 eV excitation, (b) TA spectra of WS₂/Gr heterostructure following 1.55 eV excitation [9].

1.2.2.2. Interfacial charge transfer process at the interface of WS₂/Gr heterostructure (in above A-exciton excitation regime)

Secondly, we discuss the CT process when both graphene and WS₂ are excited, namely above the A-exciton excitation regime. The photoexcitation above the A-exciton resonance of WS₂ increases the interlayer charge transfer transitions [45]. The static screening from graphene increases the linear absorption of WS₂ however, this change in the linear absorption is not significant [44]. Despite the WS₂ following the above A-exciton excitation has photogenerated electrons with higher energy than it has upon sub A-exciton excitation, their contribution to the charge transfer process is low this is because the absorption of graphene is much weaker than the WS₂ [9]. In this regime, a hole transfer mechanism, in which photogenerated holes in the valence band of WS₂ recombined with the valence band electrons in graphene (i.e. π -band), has been proposed and supported by THz spectroscopy [9] and time-resolved ARPES (Angle-resolved photoemission spectroscopy) [43]. For the THz study, the hole transfer mechanism is supported by long-lived photoconductivity in graphene, which suggests a down-shift of the Fermi level in graphene. Such a shift is captured as well by time-resolved ARPES as shown in. figure (1.5) which shows the ultrafast depopulation of the states of graphene and WS₂. Following the photoexcitation, on the graphene side, shown in figure (1.5b, red line), there is a short-lived (~ 0.18 ps) gain of electrons above its Fermi energy. This gain turns to a long-lived (~ 2 ps) loss of electrons above the Fermi energy at 0.4 ps. However, on the side of WS₂, there is a gain in the conduction

band of WS₂ as shown in figure (1.5a), which is in line with the hole transfer from WS₂ to the graphene process [43]

In the WS₂/Gr heterostructure, the electrons and holes prefer to be energetically in the Fermi level of the metallic graphene layer, therefore they experience rapid transfer from and to the graphene π -band. The hole transfer is faster (< 0.2 ps) and more efficient than the electron transfer (~ 1 ps) due to the presence of a larger number of the hole in final states than the electrons. This leads to relativistic band energy alignments for both the WS₂ and graphene following the photoexcitation. The large separation energy (~ 1.3 eV) between the Fermi energy of graphene and the valence band of WS₂, promotes the thermalized hot holes (the holes that have energy larger than the energy barrier) to be injected in a smaller proportion from WS₂ to graphene than the hot electron injection from graphene to the conduction band of WS₂ (figure 1.5a) [9], [52]. The loss of the electrons in the valence band of graphene shown in figure (1.5b, blue line), is consistent with the hole transfer dynamics proposed by the THz [9]. It is also observed that there are no holes exist in the valence band of the WS₂ (figure 1.5c), indicating the ultrafast refilling or electron-injection from the π -band of the graphene on a short time scale.

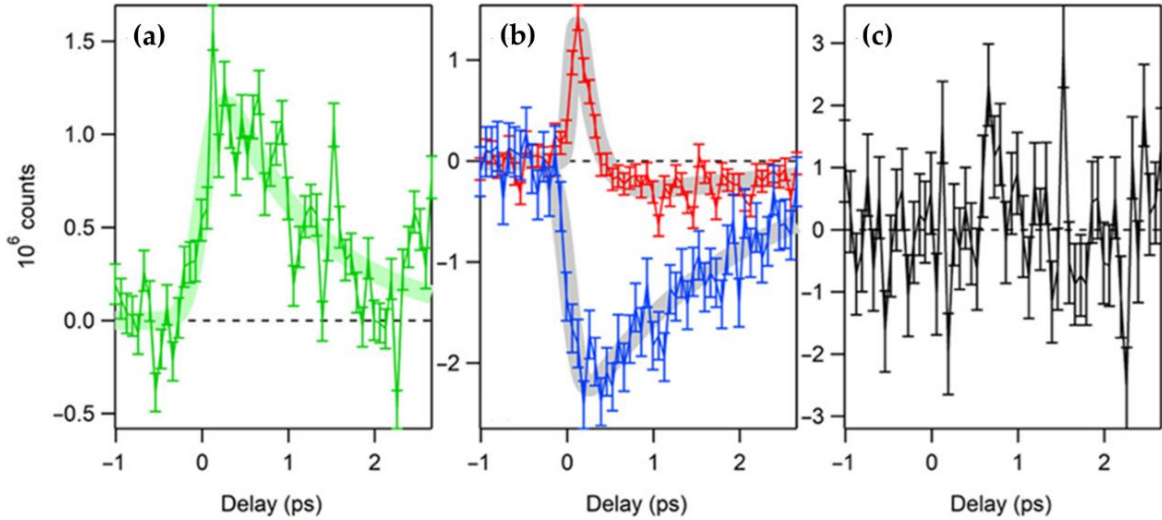


Figure 1.5: The ultrafast population of the states of graphene and WS₂ following photoexcitation, captured by time-resolved ARPES. (a) photoinduced charge carrier population in the conduction band of WS₂, showing a gain of electrons of ~ 1.2 ps lifetime, indicating electron injection from graphene to WS₂, (b) transient charge carrier depopulation in graphene below the Fermi energy (blue), showing a loss of electron with ~ 1.8 ps lifetime and above the Fermi energy (red), the short-lived (~ 0.18 ps) gain of electrons turns to a long-lived (~ 2 ps) loss of electrons, (c) the transient charge carrier population in the valence band of WS₂, indicating the ultrafast refilling or electron-injection from the π -band of the graphene on a short time scale [43].

2. Terahertz spectroscopy

The proposed research questions of the thesis are addressed by time-resolved terahertz spectroscopy (TRTS). In a typical THz spectroscopic study, two pulse lasers are used: one to excite the sample for charge carrier generation and the other to probe the pump-induced photoconductivity dynamics of the sample. These two lasers arrive at the sample in a controlled delay time. This delay time allows the measurement of the photoinduced change in conductivity as a function of time.

A unique advantage for TRTS lies in the fact that the electromagnetic field of the THz probe pulse can be mapped out by a third laser pulse by electro-optical sampling method in the time domain. Since the phase information is not lost, TRTS can directly access the material parameters such as complex conductivity, mobility, and refractive index with and without optical excitation. This contrasts with some other optical tools where only the intensity is measured, and the phase information is lost for a pulse.

This chapter gives a short overview of the components, the physical principles of this technique, and the material properties that can be extracted from the spectra.

2.1. Terahertz radiation

Terahertz radiation lies between the far- and mid-infrared regions in the electromagnetic spectrum. The region, in which the THz range can be implemented in applications between electronics and optics and is called the THz gap. The THz light has low photon energy (0.4-40 meV) and a sub-mm wavelength (3 mm-30 μm) corresponding to a frequency in the range of 0.1-10 THz. This characteristic energy scale of THz makes it suitable for semiconductor technology and condensed matter physics as it provides a direct probe to low energy excitations in materials including but limited to the rotational transition of molecules, electronic motion in solid, low-frequency phonon modes, charge ordering, and superconducting gaps in superconductors [51]-[54]. As the THz wave is very short (few ps), it is difficult to be electronically recorded either by oscilloscope because its bandwidth reaches only several GHz or by bolometer that will be overwhelmed by the black body radiation which corresponding to 6 THz at room temperature. This difficulty of detection and generation of THz has been resolved thanks to the development in the ultrashort laser pulses and the nonlinear optical tools by the end of the 1980s. Since then, the limit of the THz time-domain has extended to the near-infrared region (100 THz, 3 μm) and hence could provide a picosecond resolution for the free carriers near their equilibrium state [54]. When the photon energy is larger than the bandgap, the carriers below the Fermi level contribute to the optical response via the interband electronic transition. In contrast, the small photon energy of THz ($h\nu \sim 0.004$ eV for 1 THz) stimulates the electronic transition near the Fermi edge and the probed free carriers contribute to the electrical conductivity [54]. The electric field of the THz pulse is generated via difference-frequency generation where two different frequencies from the amplified laser spectrum cross a nonlinear medium, creating a nonlinear polarization with a resultant difference of the two frequencies (more details in section 2.4.1.1). The THz is detected by an electro-optical sampling technique that records the electric field in the time domain and gives information about the complex dielectric function of the sample (section 2.4.2.) naming this spectroscopy “THz time-domain spectroscopy” (THz-TDS).

2.2. Terahertz setup

The THz setup is shown in detail in figure (2.1). Here a commercial, regenerative amplified, mode-locked Ti: sapphire femtosecond laser operating with central energy of 1.55 eV (800 nm), a pulse length of 50 fs, and a repeating frequency of 1 kHz is employed for the THz spectrometer. A beam splitter splits the laser into two before it enters the THz setup. The first pulse is for pumping the sample. The second pulse is further split into two beams: the one with the majority energy is used to generate the

THz field for probing the charge carrier dynamics; the other with weak energy (so-called sampling beam) is utilized to map out the THz field intensity generated by the beam 1. The arrival of the pump and probe pulses to the sample is controlled by a delay stage which changes the path length of the pump.

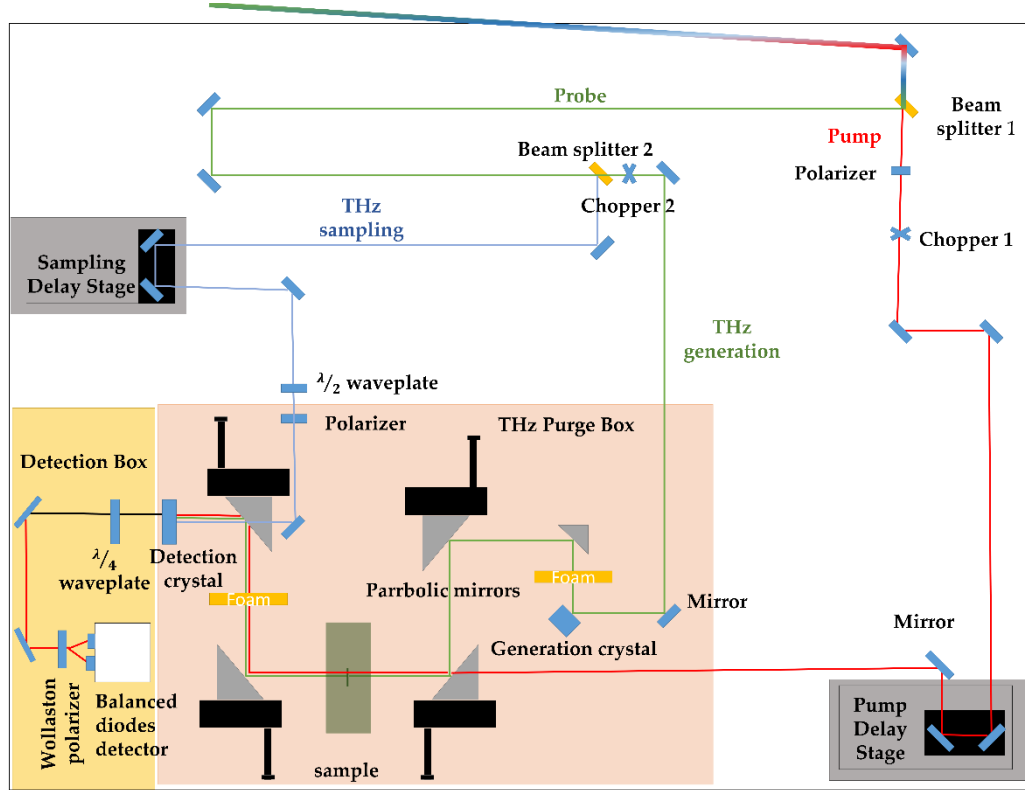


Figure 2.1: The sketch of the Terahertz setup.

Let us look first at the pump beamline (red beamline). Before the light falls into the delay stage, it passes through a polarizer to filter out the undefined or mixed polarized beams and then to a chopper that is used to record the photo-induced change of the THz waveform in the pump-probe measurement. The pump beam reaches the sample by passing through a 5 mm hole in the parabolic mirror. To ensure that only the THz beam passes, a foam is placed to block the propagation of the pump beam.

The second beamline is the probe beam of diameter ~ 5 mm (green beamline). This beam is further split into two beams, one for THz generation (green beamline) and the other for THz sampling (blue beamline). When a small fraction of the 800 nm pulse falls into a 1 mm ZnTe crystal, single-cycle THz pulses of ~ 1 ps duration, covering the range of 0.4-2 THz is generated. This THz pulse focuses on the sample via a pair of off-axis parabolic mirrors. The generated THz and the sampling beam, that generated from the oscillator in the laser system collimate and refocus on a 0.5 mm thickness

ZnTe sampling crystal. By changing the delay time between the 800 nm sampling pulse and the THz pulse, the temporal profile of the THz waveform is mapped out [55]. The light coming out from the laser is linearly polarized and may lose its polarization when it travels through the air. Therefore, a polarizer is placed to re-linearize the laser beam before falling into the ZnTe detection crystal (EO crystal). The THz detection occurs via the electro-optic sampling effect (more details in section 2.4.2) through changing the detection beam polarization through changing the EO crystal refractive index. The THz beam makes birefringence in the EO crystal, changing the polarization of the 800 nm laser beam from linear to elliptical after a quarter-wave plate. The elliptically polarized beam splits into two beams with unequal intensities by Wollaston prism. Due to the induced birefringence of the THz field, the intensity difference is measured by two balanced diodes. The whole THz beamline is enclosed and purged by nitrogen to avoid water absorption. The measurements in this study are performed under ambient conditions and at room temperature.

2.3. Measurement techniques

2.3.1. THz time-domain spectroscopy (THz-TDS)

In our sample (WS₂/Gr heterostructure), the THz-TDS technique can be used to measure the complex THz field (amplitude and phase) and investigate the complex material parameters (complex conductivity, refractive index, mobility, permittivity, etc.) in the far-infrared range without using Kramers-Kronig transformation. For example, the initial Fermi energy and the initial carrier density (before the photoexcitation) can be determined by using THz-time domain spectroscopy. In a typical study, the transmitted THz probe is measured as the temporal evolution of the electric field by monitoring the detection delay. The THz waveform is recorded in the time domain for both the substrate (WS₂/ sapphire) $E_0(t)$ and the graphene on the substrate (sapphire/WS₂/Gr), $E(t)$. Through the Fourier transformation, these time-dependent THz waveforms $E_0(t)$ and $E(t)$ can be transformed into the frequency-dependent THz waveforms $E_0(\omega)$ and $E(\omega)$ that can be used to determine the complex sheet conductivity $\sigma(\omega)$ of the graphene via:

$$\frac{E(\omega)}{E_0(\omega)} = \frac{n+1}{n+1+Z_0\sigma(\omega)} \quad (2.1)$$

Here, n is the refractive index of the substrate in the THz frequency and Z_0 is the impedance of the free space (377 Ω). From the fitting of the complex sheet conductivity

with the simple Drude model, we can get the value of the Drude weight D and scattering rate Γ :

$$\sigma(\omega) = \frac{D}{\pi} \frac{1}{(\Gamma - i\omega)} \quad (2.2)$$

where ω is the angular frequency. From the Drude weight, we can determine the initial carrier density through:

$$D = (v_F e^2 / \hbar) (\pi N)^{1/2} \quad (2.3)$$

From the carrier density, we can determine the Fermi energy following:

$$|E_F|(\text{eV}) = \hbar v_F (\pi |N|)^{1/2} \quad (2.4)$$

The photoinduced carrier photoconductivity and its dynamics can be measured by pumping the sample then probing the photoinduced dynamics by a THz beam as a function of time which is controlled by a delay stage τ . To obtain the density of charge carrier experienced CT, we conducted TDS measurement for both τ before the time 0 (to infer initial carrier density N), and $\tau > 10$ ps (to obtain transient carrier density N_τ in graphene). The time scale $\tau > 10$ ps is to avoid the graphene hot carrier effect. The photoinduced Drude response (Drude weight and scattering rate), can be described by the differential change of the complex conductivity without and with the photoconductivity following this equation:

$$\Delta\sigma_\tau(\omega) = \sigma_\tau(\omega) - \sigma(\omega) = \frac{D_\tau}{\pi} \frac{1}{(\Gamma_\tau - i\omega)} - \frac{D}{\pi} \frac{1}{(\Gamma - i\omega)} \quad (2.5)$$

where D and Γ are the initial Drude weight and scattering rate, respectively. D_τ and Γ_τ are the photoinduced Drude weight and scattering rate at pump-probe delay τ . Finally, the photoinduced carrier density at a time can be estimated by:

$$\Delta N_\tau = N_\tau - N \quad (2.6)$$

2.3.2. Optical-pump THz-probe spectroscopy (OPTP)

In the typical OPTP measurement, the sample (WS₂/Gr heterostructure) is pumped by a 50-fs optical pump, and the photoinduced charge carrier dynamics are probed by the THz probe beam. The photoinduced conductivity of the sample $\Delta\sigma$ is monitored by the change in the peak value transmitted electric field ΔE as a function of pump-probe delay.

$$\Delta\sigma \propto \frac{-\Delta E}{E_0} = \frac{E_{pump} - E_0}{E_0} = e \cdot \Delta(N \cdot \mu) \quad (2.7)$$

where E_{pump} is the transmitted electric field following the photoexcitation and E_0 is the transmitted electric field before the photoexcitation. The photoinduced conductivity $\Delta\sigma$ is proportional to the change in the transmitted electric field $-\Delta E$. For a given carrier density in graphene, we assumed that the modulation of mobility in graphene is small proportional to the changes in the charge carrier density ΔN .

2.4. Theory

In this section, the theoretical principles behind the generation and detection of THz will be discussed. The generation and detection are based on second-order susceptibility (χ^2) nonlinear optical processes, namely difference-frequency generation (DFG) and Pockels effect, respectively. To understand the transmission and reflection of THz pulse, Fresnel equations are applied to calculate the dielectric function of the sample which can determine its frequency-dependent conductivity [54].

2.4.1. THz generation

The THz radiation is generated as a result of the nonlinear polarization of Ti: sapphire laser. This high-intensity femtosecond laser pulse allows the difference-frequency generation [54]. Figure (2.2) shows the THz generation by difference-frequency generation. The difference of a pair of laser frequencies creates a nonlinear polarization which is then proportional to square the difference in the frequency. The THz probe pulse can be generated through three processes: optical rectification, photoconductive switches, and laser-ionized plasma.

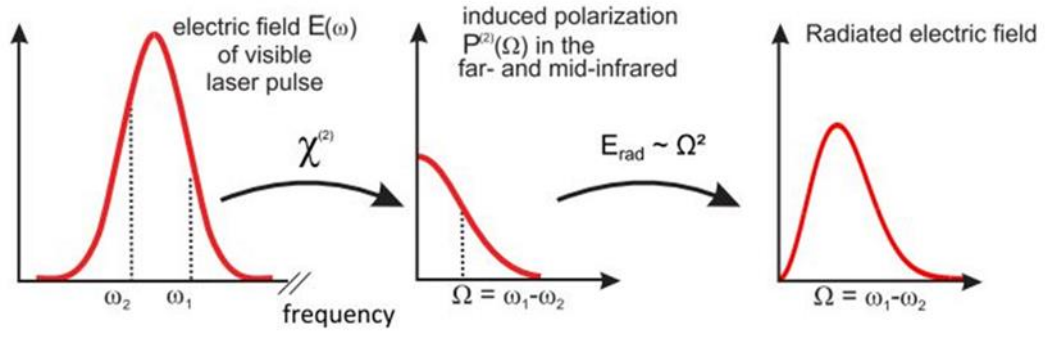


Figure 2.2: The principle of difference frequency generation (DFG) in the THz generation process [54].

2.4.1.1. Optical rectification

The optical rectification is a second-order, non-resonant, and nonlinear optical process in which the bandwidth of the generated THz is limited by the laser excitation pulse. The THz pulse is generated when 10% of the incident femtosecond optical laser propagates through the nonlinear generation crystal, causing a low-frequency polarization of the light, and hence emits the THz beam [53]. The generation crystal used here is ZnTe, which covers 0-3 THz. Materials that are used for the THz generation require to meet the following criteria [52].

1. A large nonlinear susceptibility.
2. High photostability.
3. Transparent throughout the whole desired THz frequencies and optical regimes. For example: ZnTe (0-3 THz), GaP (2-7 THz), GaSe (8-40 THz)
4. The phase-matching should be fulfilled, as the THz electric field has to propagate in a medium of definite thickness. Therefore, the phase velocity of the generated THz components should match the group velocity of the laser excitation pulse.

The nonlinear polarization (P^{nl}), which results from the difference-generation frequency (DFG), describes the dependence of electric susceptibility (χ) on the electric field (E) [54].

$$P^{nl} = E[\chi + \chi_2 E + \chi_3 E^2 + \dots] \quad (2.8)$$

The THz generation occurs via second-order nonlinear polarization, where the laser pulse has wide different frequencies fulfilling the phase-matching condition ($\Delta\omega$ or $\Omega = \omega_1 - \omega_2$ as shown in figure (2.2)).

$$P^2(\omega) = E \int d\omega_1 d\omega_2 \chi^2(\Omega; \omega_1, -\omega_2) E(\omega_1) E^*(\omega_2) \quad (2.9)$$

where the second-order susceptibility is:

$$\chi^2(\Omega; \omega_1, -\omega_2) = \chi^2(\omega_1, -\omega_2) \delta(\Omega - |\omega_1, -\omega_2|) \quad (2.10)$$

The electric field of the emitted THz is proportional to the square of the laser frequency and the nonlinear polarization.

$$E(\Omega) \sim \Omega^2 \cdot P^2(\Omega) \quad (2.11)$$

In the frequency domain, the wide frequency range corresponds to a very short laser pulse that is described as a Gauss function of time variance (σt^2) and mean frequency (ω_0)

$$E(\omega) \propto \exp\left(-\frac{(\omega - \omega_0)^2}{2\sigma t^2}\right) \quad (2.12)$$

In the time domain, the electric field is considered as a harmonic oscillating. Taking the two frequencies in figure (2.2) as an example, the electric fields will be:

$$\begin{aligned} E_1(t) &= E_0 \cos(\omega_1 t) \\ E_2(t) &= E_0 \cos(\omega_2 t) \end{aligned}$$

The second-order nonlinear polarization becomes:

$$\begin{aligned} P^2(t) &= \chi_2 E_1(t) E_2(t) = \chi_2 E_0^2 \cos(\omega_1 t) \cos(\omega_2 t) \\ &= \chi_2 \frac{E_0^2}{2} [\cos(\omega_1 - \omega_2)t + \cos(\omega_1 + \omega_2)t] \end{aligned} \quad (2.13)$$

The THz radiation is generated through the difference-frequency generation and the ZnTe generation crystal does not produce the sum frequency radiation [56].

2.4.1.2. Photoconductivity

The generation of THz field by photoconductivity switch is a resonant optical process. When the incident photon energy is larger than the bandgap, the electrons are promoted from the valence band to the conduction band. The electrons are accelerated via an external applied DC bias to the depletion region in the semiconductor, generating polarized THz radiation. The frequency of the emitted THz light depends on the lifetime of the photoconductivity process. In other words, the THz frequency is proportional to the first-time derivative of the transient current that forms it when the external bias is applied. That means the transient current depends on the strength of the laser optical excitation pulse and how long the charge carriers scatter and recombine [52]. Photoconductive semiconductors such as ion-implanted GaAs and silicon should be defect-rich to reduce the fall time of the transient current. The photoconductive antenna is an example of the photoconductive switches that consist of devices with μm semiconductor electrodes. These electrodes generate a high spectral weight at low frequencies (up to 0.1 THz) [52].

2.4.1.3. Plasma generation

THz radiation can be generated by plasma generation through ionization tunneling of the laser where the electrons are accelerated, broadening the laser radiation. For instance, a laser of 800 nm generates a 400 nm light when it passes through BBO nonlinear crystal. This second harmonic 400 nm beam and the remaining 800 nm light mix in the air, creating a fluence beyond the air ionization threshold. This process accelerates the ionized electrons due to the asymmetry electric field of the second harmonic light, generating a THz pulse.

2.4.2. THz detection by electro-optic sampling

In the ZnTe detection crystal, the 800 nm sampling beam overlaps with the THz beam. The electric field of the THz beam makes a birefringence in the crystal without inversion symmetry, causing a rotation in the sampling beam polarization from linear to elliptical. This birefringence is caused because both the THz frequency and the visible light frequency propagate in the crystal at the same speed. The change in refractive index in detection crystal with the presence of THz electric field is called linear electro-optic effect or Pockels effect [53], [54]. The electro-optic effect is a second-order susceptibility (χ^2) and the THz electric field and the laser optical field cause a nonlinear polarization. The electric field and magnetic field of electromagnetic

waves propagating in the air are perpendicular to the direction of the wave propagation. The direction of propagation is a superposition of the two waves in different directions. Suppose the electric field propagates in the z-direction is a superposition of the two electric field waves in y- and x- directions. The light coming from the laser is linear polarized that means the phase shift of the two waves in the x- and y- direction is zero. After the detection crystal, a phase shift happens due to the induced birefringence of THz radiation in the crystal that makes the refractive index to be different for x- and y- polarized light. The outcoming laser ends up with a circular (if the phase shift is $\frac{\pi}{2}$ rad) or elliptical polarization (for other phase shifts). Suppose the refractive index changes in the x-direction ($n_x = n_0 + \delta n_x$, where n_0 is the initial refractive index of crystal and δn_x is the induced refractive index due to the THz birefringence) and remains constant in the y-direction ($n_y = n_0$), so the incoming electric field to the crystal is:

$$\vec{E}_{in} = A_x \hat{x}. e^{i(kz - \omega t)} + A_y \hat{y}. e^{i(kz - \omega t + \phi)} \quad (2.14)$$

Since the incoming light is linearly polarized, the phase shift ϕ is zero. After falling into the crystal, the two waves become out of phase with a factor of $k_0 \delta n_x d$ where k_0 is the wave vector of propagating waves in the air in z-direction and d is the thickness of the crystal. Therefore, the out-coming electric field becomes:

$$\vec{E}_{out} = A_x \hat{x}. e^{i(k_0(n_0 + \delta n_x)d - \omega t)} + A_y \hat{y}. e^{i(k_0 n_0 d - \omega t)} \quad (2.15)$$

The quarter-wave plate, which is placed after the detection crystal, changes the polarization of the outcoming wave. In the absence of the THz field, the detection crystal will not change polarization, but the out-coming wave after the quarter-wave plate becomes circular polarized. However, in presence of THz, it becomes elliptical as shown in figure (2.3). The phase shift ϕ of two perpendicular polarizations is:

$$\phi = \frac{2\pi d}{\lambda_{opt}} n_{opt}^3 r_{41} E_{THz} \quad (2.16)$$

where r_{41} is the electro-optic coefficient for ZnTe crystal. This phase shift splits into a beam with two polarization directions ($\hat{x} + \hat{y}$ and $\hat{x} - \hat{y}$) by Wollaston prism which transforms them into intensity as follows:

$$\sin(\phi) \approx \phi = \frac{I_1 - I_2}{I_1 + I_2} \quad (2.17)$$

The Balanced diode detector measures the intensity difference between the two beams. In case, the THz field is absent, the diodes give a zero signal (only one beam comes out), as the intensities are the same in both directions. However, in presence of THz, the diode detects an intensity difference.

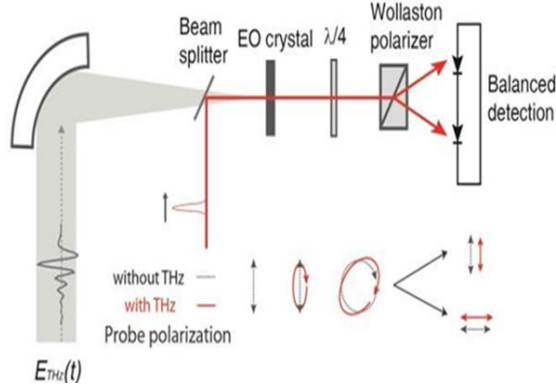


Figure 2.3: Principle of electro-optic effect in detecting the THz radiation [57].

2.5. Calculation of complex parameters from THz measurements

From THz-TDS measurement, the frequency-dependent complex parameters can be extracted such as refractive index $n(\omega)$, dielectric function $\varepsilon(\omega)$, and conductivity of material $\sigma(\omega)$. Consider, THz pulse is a plane wave with frequency-dependent electric field $E(\omega)$ propagates through the active region of the sample at distance x of complex refractive index n_x and length l_x . The initial THz waveform at the interface before passing through the sample is $E_{x-1}(\omega)$ and at the interface after transmitting through the sample is denoted by $E_{x+1}(\omega)$.

$$E_{x+1}(\omega) = E_{x-1} \cdot t_{x,x-1} \exp\left(\frac{in_x \omega l_x}{c}\right) \cdot t_{x,x+1} MR_x \quad (2.18)$$

where t is Fresnel transmission coefficient.

$$t_{x,x+1} = \frac{2n_x}{n_x + n_{x+1}} \quad (2.19)$$

where MR_x is the multiple reflections in sample x .

$$MR_x = \left[1 + r_{x-1,x} \cdot r_{x,x+1} \cdot \exp\left(\frac{2i\omega l_x}{c}\right)\right]^{-1} \quad (2.20)$$

where $r_{x,x+1}$ is the Fresnel reflection coefficient of the incident THz pulse.

$$r_{x,x+1} = \frac{n_{x+1} - n_x}{n_{x+1} + n_x} \quad (2.21)$$

In optical pump-THz probe measurements (OPTP), if the penetration depth of pump pulse is shorter than the wavelength of THz pulse and the sample thickness, the excited region is approximated by a homogenous region of length l . To explain more in detail, let us consider a pulse propagates through the air with refractive index n_1 , then through a window or cuvette of refractive index n_2 , and finally hits the sample of refractive index n_3 or n_3^* . As shown in figure (2.4), if the sample is excited, the transmitted pulse then emerges from another window or cuvette n_4 to the air of n_5 .

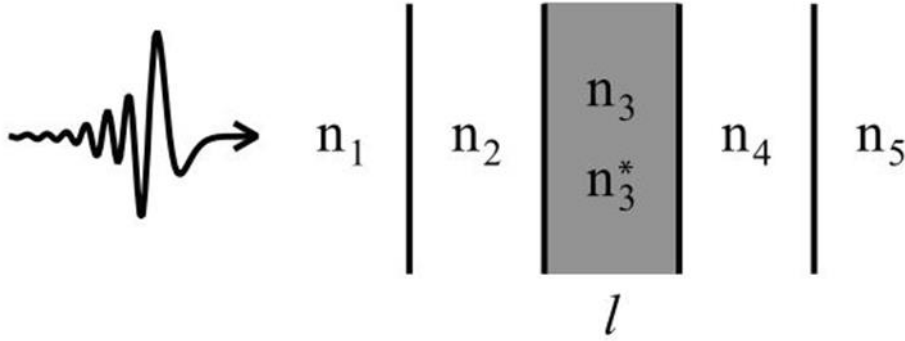


Figure 2.4: The transmission of THz field through different refractive index [53].

The transmitted THz electric field before exciting the sample is:

$$E_{unexc}^{calc}(\omega) = E_0(\omega) t_{12} e^{i\omega n_2 l_2 / c} t_{23} e^{i\omega n_3 l / c} t_{34} e^{i\omega n_4 l / c} t_{41} e^{-i\omega n_1 (l_2 + l_4 + l) / c} MR_3 \quad (2.22)$$

The transmitted THz electric field though the excited sample is:

$$E_{exc}^{calc}(\omega) = E_0(\omega) t_{12} e^{i\omega n_2 l_2 / c} t_{23}^* e^{i\omega n_3^* l / c} t_{34}^* e^{i\omega n_4 l / c} t_{41} e^{-i\omega n_1 (l_2 + l_4 + l) / c} MR_3^* \quad (2.23)$$

The strikes (*) mean the transmission and multiple reflection coefficients in the case of a photoexcited sample.

$$\frac{E_{exc}^{calc}(\omega)}{E_{unexc}^{calc}(\omega)} = \frac{t_{23}^* t_{34}^*}{t_{23} t_{34}} e^{i\omega \Delta n l / c} \frac{MR_3^*}{MR_3} \quad (2.24)$$

$$\Delta n = n_3^* - n_3 \quad (2.25)$$

When the sample is a thin film or when the pump penetration is shorter than the THz wavelength, the reflected beam can overlap in time with the transmitted beam, so the corrections MR_3^* and MR_3 are necessary. However, in solution, the samples are kept in a cuvette and the reflected beams are filtered out as the optical length is long.

In the experiment, we measure in the time domain the transmitted THz field through the unexcited sample and the photo-induced change in the field between the unexcited and excited sample. These waveforms can be resolved in the frequency domain via Fourier transform and the ratio between them related to the calculated one

$$\frac{\Delta E^{calc}(\omega)}{E_{unexc}^{calc}(\omega)} = \frac{E_{exc}^{calc}(\omega) - E_{unexc}^{calc}(\omega)}{E_{unexc}^{calc}(\omega)} \quad (2.26)$$

2.6. Conductivity models

The conductivity of the semiconductors in the THz window is determined by the behavior of the charge carriers (free or confined); originating from the material properties (carrier effective mass, heat capacity, etc.), temperature (carrier-phonon interactions), sample quality (scattering time which is affected by the number of impurities and defects per unit volume) and the carrier density (carrier-carrier interactions). This section represents some standard charge carrier transport models in the semiconductor systems.

2.6.1. Drude model

Drude model is used to describe the conductivity in the bulk semiconductors and metals due to the response of charge carrier to the THz field. It assumes that in absence of an electric field, the free carriers act as ideal gas that interacts randomly with the lattice impurities and phonons only (carrier-carrier and carrier-phonon collisions). The Drude conductivity can be expressed as follows:

$$\sigma_{Drude}(\omega) = \frac{Ne^2}{m^*} \frac{\tau_s}{(1-i\omega\tau_s)} = \frac{\epsilon_0\omega_p^2\tau_s}{(1-i\omega\tau_s)} \quad (2.27)$$

where e is the electron charge, N is the carrier density, ω_p is the plasma frequency and can be written as:

$$\sqrt{\frac{Ne^2}{m^*} \cdot \frac{1}{\epsilon_0}} = \omega_p \quad (2.28)$$

Here, ϵ_0 is the vacuum permittivity, and m^* represents the effective mass of the charge carrier. The Drude model can extract through the fitting, the scattering time which is the angular frequency at which the real and imaginary conductivity cross ($\tau_s = 1/2\pi\omega_{cross}$) as shown in figure (2.5).

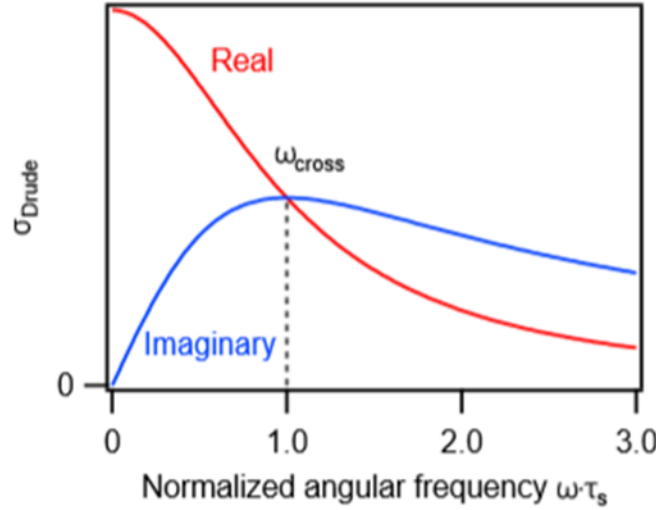


Figure 2.5: Drude conductivity with a normalized angular frequency. The scattering time is the angular frequency at which the real and imaginary conductivity cross ($\tau_s = 1/2\pi\omega_{cross}$) [53].

The real conductivity increases towards the lower frequencies and it peaks at $\omega = 0$ (where the free carrier resonance is) while the imaginary part is positive through the whole frequencies, see figure (2.5). The reason why the real conductivity peaks at $\omega = 0$ is that the force constant of the free carriers is zero. The force constant is a proportional factor of the charge displacement and its restoring force and it is the key factor that determines the position of resonance (absorption of the electromagnetic light).

2.6.2. Drude-Smith model

Although the simple Drude model is a suitable model for describing the macroscopic electrical behavior of the carriers in the semiconductors, it does not apply to all the materials, especially for nanomaterials experiencing strong spatial confinements. Drude-Smith model is an extension of the simple Drude model, considering the confinement in the conduction of free charge carriers, following this equation:

$$\sigma_{Drude-smith}(\omega) = \frac{\epsilon_0 \omega_p^2 \tau_s}{(1-i\omega\tau_s)} \left(1 + \frac{C}{(1-i\omega\tau_s)}\right) \quad (2.29)$$

Here C is ranging between 0 and -1. When $C = 0$, the equation represents a random momentum scattering process, e.g. a Drude response. However, in the Drude-smith model, $C = -1$ which describes a complete backward scattering event.

Drude-Smith model succeeds in describing the conductivity at the surface, boundaries, and the edges of the materials, where backward scattering happens

2.6.3. Lorentz oscillator model

Lorentz oscillator model is used to describe the conductivity that arises due to the response of bounded carriers, e.g. excitons. This model is suitable in describing the conductivity of e.g. quantum dots, or monolayer TMDCs, where the exciton effect prevails. The exciton resonance resulted from intraband transitions of electron and hole, and it is different from the free carrier resonance that positioned at $\omega_0 = 0$. The resonance energy is determined by the distance between the energy levels, e.g. the splitting between 1S and 2P exciton states.

Lorentz oscillator model considers the system as a resonance oscillator of angular frequency ω_0 and introduces a restoring force parameter to the Drude complex conductivity. The conductivity becomes:

$$\sigma_{Lorentz}(\omega) = \frac{\epsilon_0 \omega_p^2 \tau_s}{(1-i\omega\tau_s + i\tau_s\omega_0^2/\omega)} \quad (2.30)$$

3. Experiments and results

3.1. Device fabrication and characterization

Two sapphire/WS₂/Gr samples (named as sample A and sample B, respectively) are used in this study. The monolayer WS₂ on the sapphire substrate is purchased from six carbon Technology Shenzhen and is produced by chemical vapor deposition (CVD) methods. The WS₂/Gr heterostructure is fabricated via wet transferring CVD-grown monolayer graphene on top of the WS₂ monolayer grown on sapphire. Details for the graphene transfer process can be found in section 1 in supporting information (SI).

Here we employed the ionic gating method (see details in SI) to control the Fermi level in graphene, to investigate the role of Fermi level on the interfacial charge carrier dynamics at WS₂/Gr interfaces. In short, three pairs of electrodes including the source, drain, and side-gate are defined by evaporating Cr/Au through a shadow mask on the top of the WS₂ layer. These electrical contacts enable the control over the charge carrier density in graphene and the measurement of the resistance of graphene. The source, drain, and side gate are connected to the electrodes either by silver paste (sample A) or wire bonding (sample B). Sample A is shown in figure (3.1).

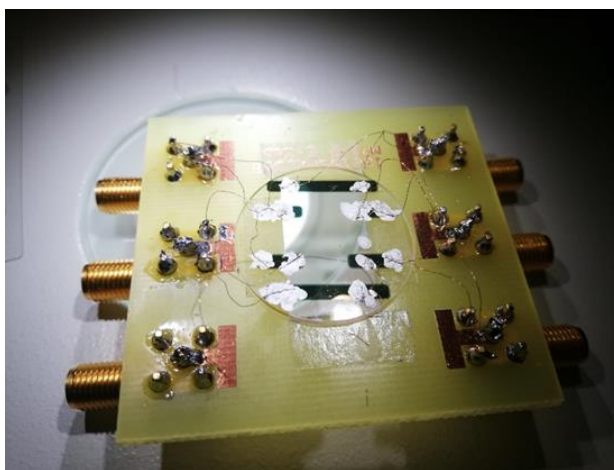


Figure 3.1: The WS₂/Gr heterostructure device by the ionic gating technique.

Prior to studying the ultrafast carrier dynamics, static optical and electronic properties of the heterostructure are investigated via UV-vis absorption and Raman spectroscopy. From the UV-vis absorption spectra in figure (3.2a) for sample A and figure (S1.b) for sample B, the two exciton resonances of WS₂, namely A- and B-exciton are observed at ~ 2 eV and ~ 2.4 eV respectively. These exciton transitions result from the spin-orbit splitting in the valence band of WS₂ at the *K*-point in the Brillouin zone. The featureless absorption constant of graphene in the near-infrared region (~ 2.3%) is observed in the heterostructure together with the exciton resonances of the WS₂, as shown in figures (3.2a and S1.b). The Raman spectra of the heterostructure shown in figures (3.2b and S1.a) represent the characteristic vibration modes for both WS₂ and graphene. The Raman spectra confirm the monolayer nature of WS₂ and graphene. Two characteristic vibration modes of WS₂ monolayer: in-plane (E_{2g}^{-1}) and out-of-plane (A_{1g}^{-1}) are observed at ~ 357 cm⁻¹ and ~ 415 cm⁻¹, respectively, in good agreement with those for WS₂ monolayer [58]. The 2D-and G-band modes of monolayer graphene are shown at ~ 1584 cm⁻¹ and ~ 2646 cm⁻¹, respectively [23], [59].

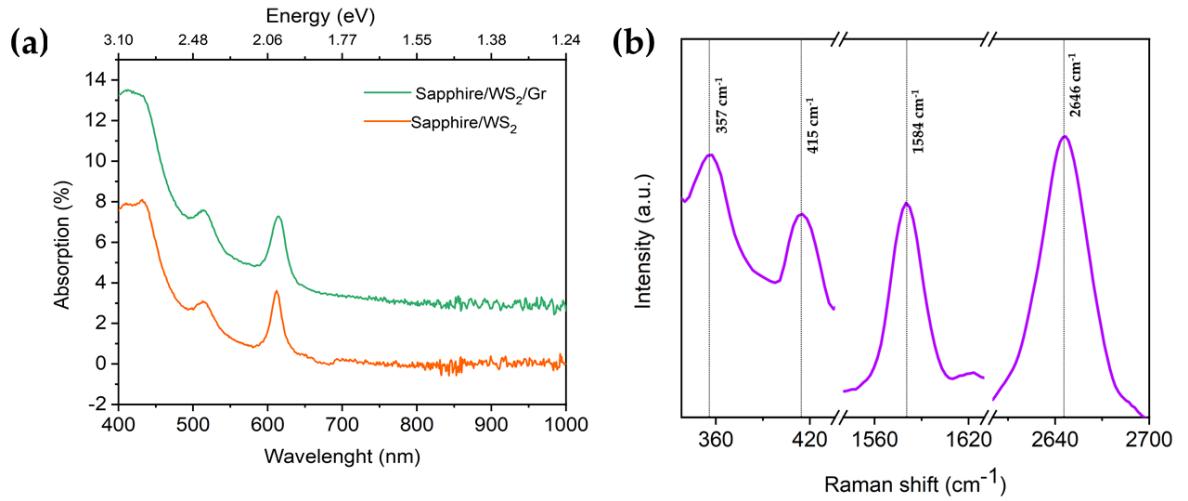


Figure 3.2: Static optical properties of WS₂/Gr heterostructure. (a) UV-vis absorption spectra of sapphire/WS₂ and sapphire/WS₂/graphene, (b) Raman spectra of one characteristic spot in the sapphire/WS₂/graphene sample.

3.2. In situ electrical and OPTP measurements

This work aims to understand and tune the charge carrier transfer dynamics in WS₂/Gr heterostructure by tuning the Fermi level in graphene. For that, we perform OPTP measurement on an ionic-gated WS₂/Gr heterostructure and simultaneously monitor the resistance change in graphene via four-point probe measurements. The sample is gated by a sweeping potential, from -3 V to +3 V, with a scan rate of 0.4 mV/s. As shown in figures (3.3a and S2.a), the resistance is low at both p- and n-doped graphene which confirms the metallic behavior of highly-doped graphene. The resistance reaches the maximum at the charge neutral point (CNP) of graphene, where the charge carrier density in graphene vanishes, representing the semiconductor like-behavior of graphene. These results indicate the successful tuning of Fermi energy level in graphene. With negative gate voltages, holes are responsible for the conduction, (i.e., graphene becomes p-doped); and vice versa, with positive gate voltages, electrons are responsible for the conduction (graphene becomes n-doped).

Now we focus on the THz conductivity of the WS₂/Gr heterostructure. The photogenerated charge carrier dynamics in graphene and WS₂/Gr heterostructure are investigated by optical-pump THz-probe (OPTP) spectroscopy. In a typical OPTP measurement, an optical pump of ~ 50 fs duration excites graphene only with 800 nm excitation (sub-A exciton resonance of WS₂) and THz pulses probe the pump-induced photoconductivity ($\Delta\sigma$). The change in the transmitted electric field (ΔE) upon the photoexcitation is measured as a function of pump-probe delay (more details in chapter 2). The pump-induced photoconductivity is proportional to the change in the transmitted electric field ($\Delta\sigma \sim -\Delta E$).

As discussed in chapter 1, the dynamics of the heterostructure in the sub-10 ps are dominated by the hot state of the graphene electronic system. Photoconductivity (for both n- and p-doped) shows a negative conductivity (e.g. photo-induced THz transparency) for doped graphene, and a positive sign for intrinsic, un-doped graphene (e.g. photo-induced THz absorption). While sample B shows the results following the expectation (see figures S2.b and S2.c), sample A still shows small negative photoconductivity at even Dirac point, as shown in figure (3.3b and 3.3c). The small negative photoconductivity at charge neutral point graphene observed in sample A can be rationalized by the larger local fluctuations in graphene (whose origins requires further investigation). For Fermi level close to Dirac point, although the net charge is ~0 across the sample, the photoconductivity is dominated by the local (both electron and hole) doped regimes. Despite small negative conductivity at the Dirac point for sample A, the general trend of photoconductivity at different Fermi levels further confirms the successful gating of the graphene layer in the heterostructure which is already illustrated from electrical transport data.

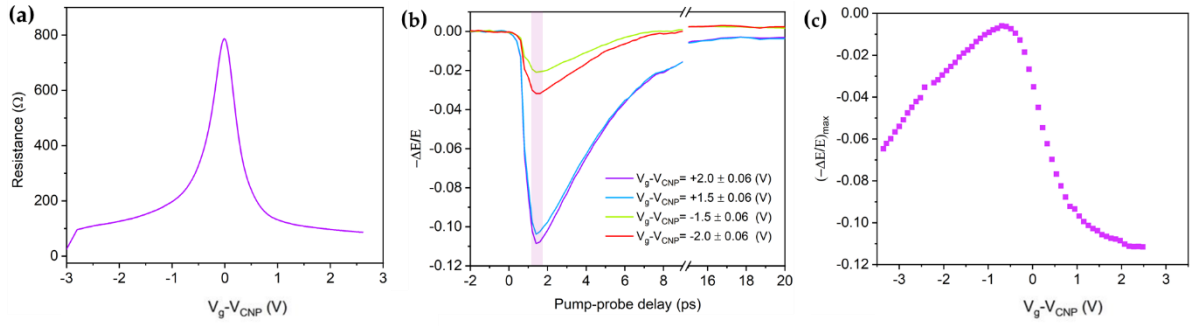


Figure 3.3: Effective tuning of Fermi energy level in graphene, confirmed by both electrical and optical measurements. (a) Resistance of graphene in the heterostructure at different gate voltages, (b) OPTP dynamics of WS₂/Gr heterostructure following 800 nm photoexcitation at different gate voltages (c) maximum photoconductivity at ~ 1.4 ps as a function of gate voltages (for sample A).

3.3. Discussions and results

Discussion 1: The interfacial charge transfer process at varied graphene Fermi levels

The first point of interest here is how the tuning of the Fermi level in graphene affects the interfacial charge transfer (CT) between the graphene and WS₂ layer. Following the CT process, the charge carrier density in both graphene and WS₂ is transiently modulated, and hence the photoconductivity of the heterostructure changes. However, the mobility of charge carriers in graphene is at least two orders of magnitude higher than WS₂. This means the photoconductivity signal in the WS₂/Gr heterostructure is fully dominated by the changes in conductivity (e.g. by the change of charge carrier density) in graphene following CT. Here, we focus on the CT process following the 800 nm excitation, where only the graphene layer is excited. As discussed earlier in chapter 1 in this thesis that upon the 800 nm photoexcitation, the hot carriers generated in graphene can be injected into WS₂. However, it remains highly debated how the injection takes place. According to the literature, two scenarios have been proposed: (1) direct hot-electron transfer, where the hot electrons are injected directly from graphene to WS₂ before the thermalization process [10]. In this scenario, the hot electron transfer rate should be extremely fast, competing with the thermalization process in graphene. (2) photo-thermionic emission (PTE), in which only the thermalized hot carriers that have sufficient energy above the Schottky barrier can be injected from graphene to WS₂ [9], [46]. One critical parameter that can differentiate these two scenarios is the dependence of CT efficiency on the Fermi level in graphene.

In the direct hot electron injection scenario, the CT efficiency is expected to be independent of the Fermi level of graphene. However, in the PTE scenario, the CT efficiency strongly depends on the Fermi level of graphene. This is because the PTE efficiency is governed by two critical parameters, i.e. Schottky barrier (the energy barrier for HET) and heating efficiency (the fraction of absorbed energy from incident light that is transferred to the electron system). Both of Schottky barrier and heating efficiency vary at different Fermi levels in graphene. Therefore, to determine whether scenario (1) or (2) or both contribute to the CT process, we monitor the magnitude of the conductivity change in graphene, as a consequence of charge carrier injection from graphene to WS₂, under varied gating voltages (and hence varied graphene Fermi levels).

As discussed before, in the sub-10 ps time scale, the photoconductivity is dominant by the hot carrier response in graphene itself. Moving further to the later time scale, the signal is dominant by the conductivity changes following optical excitation and CT. In figure (3.4a), we plot the photoconductivity dynamics from 15 ps on, to discuss the CT process. In general, it is shown that p-doped graphene exhibits positive photoconductivity, and n-doped graphene exhibits negative photoconductivity upon photoexcitation and ultrafast charge transfer. Based on these results, we can conclude that in both doping regimes, electrons are always injected from graphene to WS₂. For p- (or n-) doped graphene, losing electrons results in an increase (or a decrease) of charge carrier density at the Fermi surfaces. This results in a transient enhancement of conductivity for p-doped graphene, and transient conductivity reduction for n-doped graphene. In figure (3.4b), we plot the photoconductivity at ~ 20 ps after photoexcitation (for both samples A and B) as a function of the gate voltage V_g (relative to the charge neutral point voltage V_{CNP}). We find that the photoconductivity is close to 0 in the highly p-doped regime. This observation rules out the contribution of non-thermalized HET as the dominant CT mechanism. Also, this ~ 0% CT signal cannot be assigned to the doping-induced Pauli blocking effect in graphene (taking place when $E_f > \hbar\nu/2$), as for the doping regime achieved in the studies, the Fermi level (E_f) in graphene is still much lower than what Pauli blocking will take place ($E_f > \hbar\nu/2$). Sample B, limited by the gating efficiency, still shows a finite CT signal even for the most p-doped regime. But the overall trend for both samples is consistent, i.e. CT efficiency decreases with increasing the hole doping. Such doping or Fermi level-dependent CT efficiency can be simply captured by the PTE effect. By gating graphene, we are tuning both the interfacial energy barrier and electron temperature following $(-\Delta E/E)_{max} \sim \Delta\sigma \sim \Delta N \sim e^{\frac{-\varphi_B}{k_B T_e}}$ (φ_B is the energy barrier and T_e is electron temperature). Here for the first approximation, we assumed that the mobility of graphene does not change much after hot electron transfer. For the very p-doped graphene sample, a small or negligible CT signal is expected. This is because, in this doping regime, the

energy barrier for hot electron transfer is too high. With increasing the Fermi energy, HET efficiency increases, as the Fermi level gradually shifts to a lower energy barrier. When the doping increases further to achieve n-doping in graphene, efficient HET from graphene will lead to a reduction in electron density in graphene, resulting in a negative conductivity. The CT efficiency at different Fermi energies shown in figure (3.4b) is in line with these expectations.

To further support our claim of the PTE effect is dominating the HET at WS_2/Gr interface, we have further simulated the relative percentage of hot electrons above the Schottky barrier, at different Fermi levels in graphene. Briefly, we calculate the resultant hot electron distribution following photoexcitation and thermalization processes (see section 2 in SI for the simulation details) with a given fluence at different Fermi levels. Subsequently, we estimate the hot carrier density above the Schottky barrier, as shown in section 2 in SI and figure (S3). Here, we assume 100% HET efficiency for the discussion. As we can see, the simple simulation captures the main feature of CT at different gating potentials: CT efficiency is found to be 0% for the highly p-doped sample, and gradually increases to a finite positive value with less p-doping in graphene. Finally, the photoconductivity changes the sign to negative when the graphene is n-doped. Despite the good agreement in the CT efficiency trend, we do observe a relatively large deviation at the n-doped side. The simulated results show a large dependence of CT efficiency on Fermi level in graphene, which contrasts with the saturation as shown in the experimental results in figure 3.4b. Such deviation maybe because in the simulation, we have neglect some other possible CT pathways, e.g. electron injection from the filled defects to the hot hole following optical excitation (see the discussion in the next section, which provides some hint for such processes). Further investigation is certainly needed to clarify this issue. All in all, the result and discussion here provide a strong indication that the injection of thermalized hot electrons governs the HET from graphene to WS_2 .

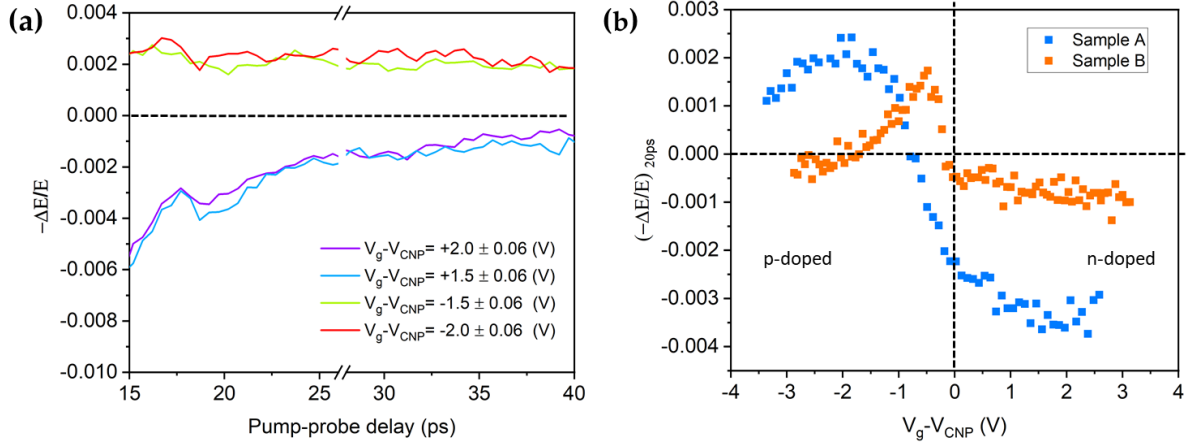


Figure 3.4: (a) OPTP dynamics in WS_2/Gr heterostructure (in sample A) at different gate voltages after carrier cooling in graphene following 800 nm photoexcitation, (b) The positive photoconductivity at time scale 20.2 ps for both samples A and B as a function of gate voltages.

Discussion 2: The interfacial charge recombination dynamics at varied graphene Fermi levels

The second interest is how the tuning of the Fermi levels in graphene affects the recombination process and the charge separation lifetime. As discussed in the introduction, unoccupied defects in WS_2 can trap the electrons injected from graphene to WS_2 , resulting in a long-lived photogating effect. Here we would like to further shed the light on the process and to explore if and how we can modulate the photogating processes. For that, we sweep the chemical potential in graphene by ionic gating, which could lead to manipulation of nature (filled or unoccupied) and density of the defects at the interfaces, when the chemical potential in graphene is resonant with the defect energy in WS_2 . We plot the long-lived recombination dynamics at different gating potential as shown in figure (3.5a). In figure (3.5b), we summarize the conductivity values at two different time ranges (42-52, vs 450-550 ps) for varied gating voltages. For p-doped graphene, when the defect states are unoccupied, the photoconductivity for both time cuts exhibit a positive long-lived photoconductivity offset. As discussed before, this is due to the photogating effect mediated by electron trapping to the empty interfacial defects, as illustrated in schematic 1. Briefly, for p-doped graphene, following 800 nm excitation, the electron injection from graphene to WS_2 causes a transient downward shift of the Fermi level. Subsequently, the injected electrons get trapped in the defect states at the interface before they recombine with the remaining

holes in graphene. The localized nature of the trapped electrons can substantially suppress the recombination rate, which leads to a long-lived (photo)gating effect in graphene. From ~ 40 ps to ~ 500 ps, the value of the positive conductivity decreases slightly, because a small amount of charge carriers is recombined in this time range. The electrons, trapped in the empty defects, are responsible for the photogating in the entire time window.

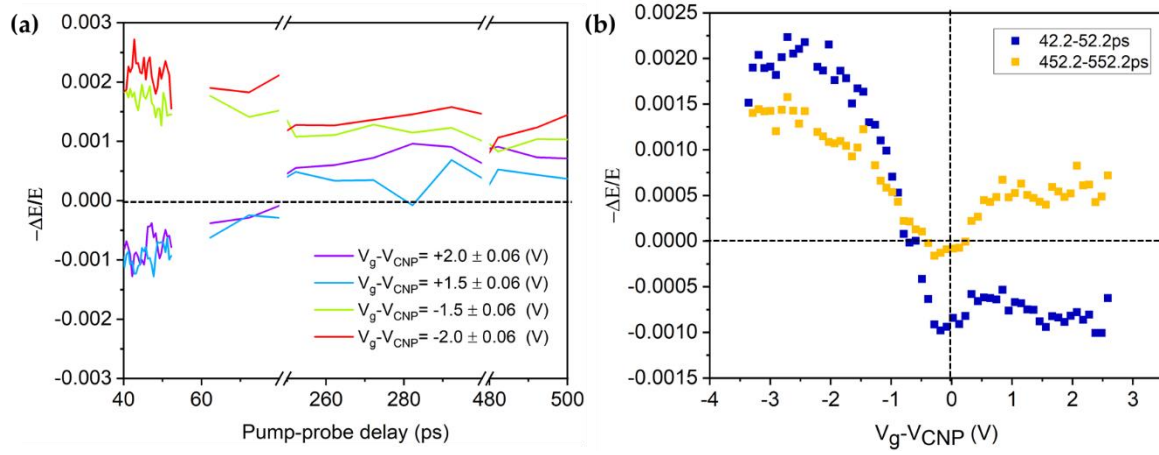
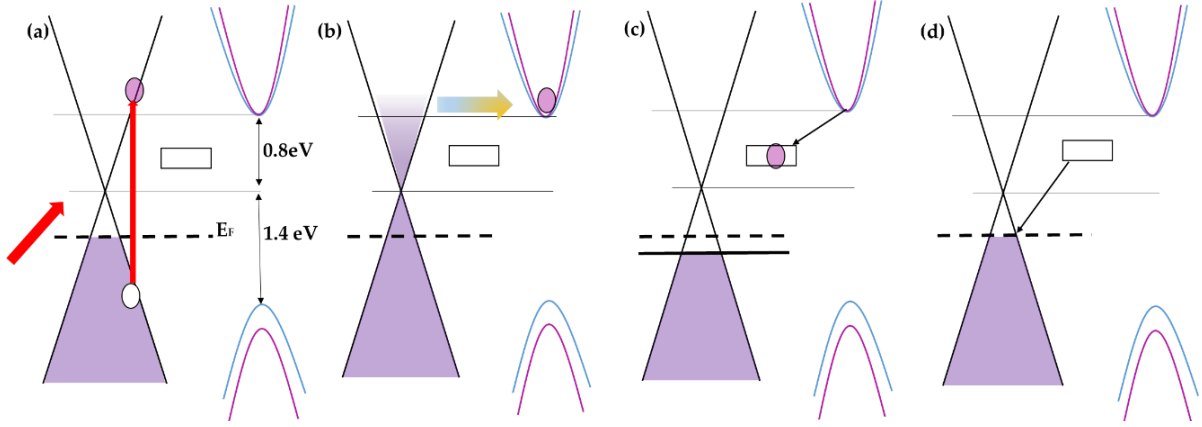


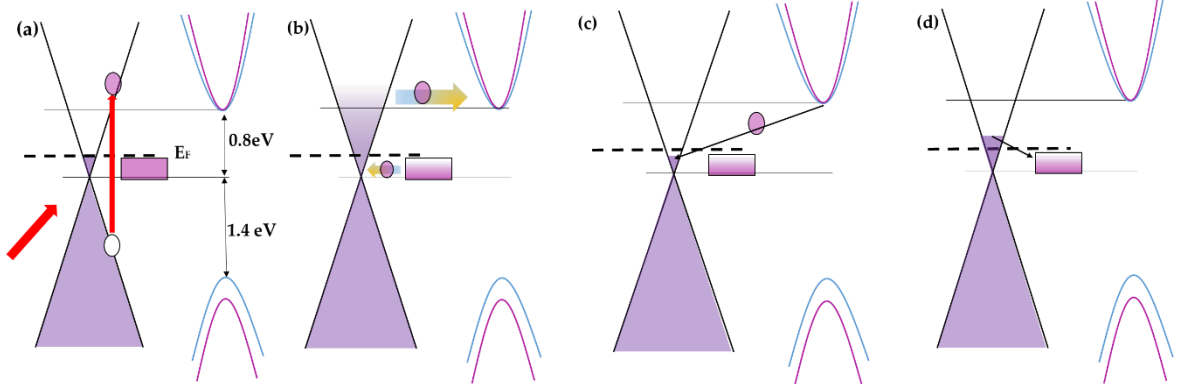
Figure 3.5: (a) OPTP dynamics in WS_2/Gr heterostructure (in sample A) at different gate voltages in longer time scale (40-500 ps) when the charge recombination happens, (b) the maximum positive photoconductivity averaged between 42.2-52.2 ps and 452.2-552.2 ps upon photoexcitation at different gate voltages.



Schematic 1: Charge carrier dynamics and recombination process at the interface of WS₂/p-doped graphene. (a) photo-excitation of graphene with 800 nm pump, (b) photo-thermionic emission effect, which leads to electron injection from graphene to the conduction band of WS₂, (c) the injected electrons from graphene to WS₂ get trapped in the empty defects, resulting in a photogating effect in the heterostructure, (d) the trapped electrons recombine with the holes in the valence band of graphene in a much longer ns time scale. After the recombination, the Fermi level returns to the initial equilibrium state.

Interestingly, in sharp contrast to the p-doped case, for n-doped graphene, the long-lived photogating effect shows an intriguing transition from large negative photoconductivity (~ 50 ps) in the early time, to a positive one to the later time scale (~ 500 ps), as shown in figure (3.5b). This result suggests a transition of photogating effect, from overall an electron gating, to a hole gating regime: that is, the WS₂ layer possesses a net negative charge accumulation (i.e. electrons) in the early time, and a net positive charge accumulation (i.e. hole) in the later time scale. Here, we rationalize such observation in a heterostructure with n-doped graphene by proposing a scenario involving defects, as depicted in schematic 2. As gradually shift up the Fermi level in graphene, the interfacial defect states can be filled electrochemically. The interfacial defect states, once filled, lost their ability to capture the injected electrons from the conduction band of WS₂. Furthermore, due to its relatively high energetics, injection of energetic hot holes from graphene to these filled defects are possible, along with the HET by PTE effect. This leads to an exchange of electrons in graphene and WS₂ (with HET from graphene to WS₂ more efficient). Therefore, in the short time scale, the net charge in WS₂ is dominant by electrons, which leads to an electron gating effect at the interfaces. In the longer time scale, as the defects are filled (with few empty holes from hot hole transfer), the electrons in the WS₂ follow a new recombination pathway compared to the p-doped case: they directly recombine with the holes in graphene. This leads to a transition from a net-electron gating regime to only a hole gating regime

supported by the filled defects. Further spectroscopic studies, e.g. by TA, are needed to fully validate our proposed scenario. Compare to the p-doped regime, we expect a much slower depopulation process from the excited states in WS₂ following CT: that is ~ 100s of ps for a back electron transfer from WS₂ to graphene for n-doped samples, vs ~ 1 ps trapping process in p-doped samples.



Schematic 2: Charge carrier dynamics and recombination process at the interface of WS₂/n-doped graphene. (a) photo-excitation of graphene with 800 nm pump, (b) Hot electron transfer from graphene to the conduction band of WS₂ and simultaneously hot hole transfer effect from graphene to the defects in WS₂ (or equivalently, electron injection from WS₂ defects to the hot holes) following optical excitation, (c) The injected electrons in the conduction band of WS₂ recombine with the holes in graphene, (d) after recombination, the Fermi level shifts upwards, the trapped holes in the defect states lead to a long-lived hole-gating in graphene.

3.4. Conclusion

There are two main conclusions from the thesis. First, we provide evidence that photo-thermionic emission dominates the interfacial charge transfer process at varied gating voltages (Fermi levels). Second, we show that the unoccupied defect states in the heterostructure can be electrochemically manipulated and have a substantial impact on the photogating processes. For the heterostructure with p-doped graphene, in which the interfacial defect states are unoccupied, defects can effectively capture the injected hot electrons from the conduction band of WS₂. This leads to a photogating effect by the trapped electrons. On the other hand, for the heterostructure with n-doped graphene, where the defects are filled electrochemically, we reported a switching in the photogating mechanism: we show that electrons are responsible for the early time (10s of ps) for photogating, which gradually switched to a long-lived photogating hole-gating processes (in > 100s ps). These results provide new insights into electrical control over both CT and recombination processes in TMDs/Gr heterostructures with potential applications in photodetection

3.5. Supporting information

Section 1: Fabrication methods

Transferring graphene by wet transfer method

The CVD graphene is transferred on the WS₂-sapphire via the dry transfer method. To transfer the CVD monolayer graphene produced on the copper sheet, first spin coat (4000 rpm) a 30 mg/ml cellulose acetate butyrate (CAB) dissolved in ethyl acetate over the Gr/Cu then bake it at 180 °C for 3 min [60]. The CAB is proved to leave minimal polymer residue on the graphene after the transfer process [60]. The copper foil in the backside of graphene is etched by placing the CAB supported Gr/Cu sample in 1 mol/L (NH₄)₂S₂O₈ solution for 10 min. Then the sample is rinsed with di-ionized (DI) water 4 to 5 times. To complete the etching of copper, the sample is left for 2 hours. in 3mol/L of (NH₄)₂S₂O₈ solution. The etching residues are removed by rinsing the CAB-Gr with DI water 4 to 5 times. Then the sample is fished and transferred on the sapphire/WS₂ substrate. Finally, the CAB polymer layer is removed by placing the sample in acetone overnight and then isopropanol for 1 hour.

Preparation of ion gel

The ion gel which acts as an efficient dielectric for gating graphene is transparent in our THz range. The ion gel is fabricated by dissolving 1 g polyethylene oxide (PEO) and 0.3 g LiClO₄ in 10-15 ml anhydrous methanol [61]. The mixture solution is stirred (250-500 rad/min) for 30 min at 90°C. When the mixture becomes clear, it kept stirred at the same speed for > 2 hours at 60°C. The ion gel is dropped on the sapphire/WS₂/Gr sample and left overnight to dry naturally.

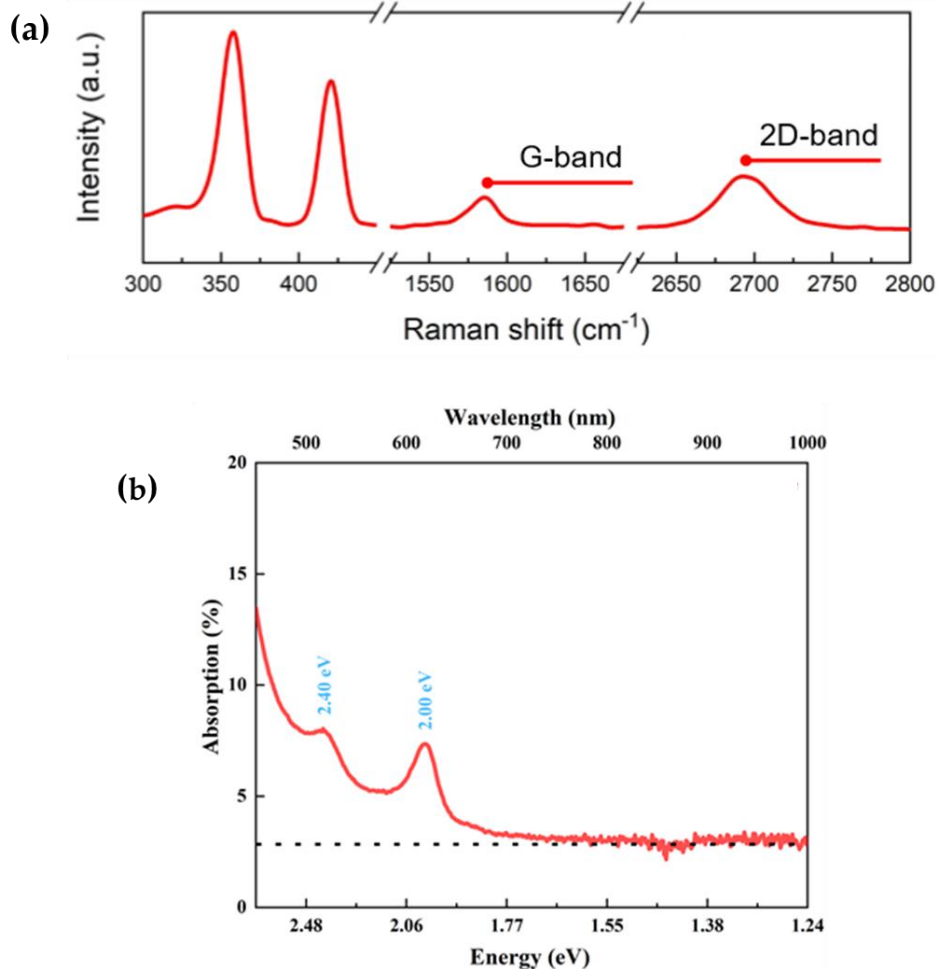


Figure S1: Static optical properties of sample B (a) UV-vis absorption spectra of sapphire/WS₂ and sapphire/WS₂/graphene, (b) Raman spectra of one characteristic spot in sapphire/WS₂/graphene.

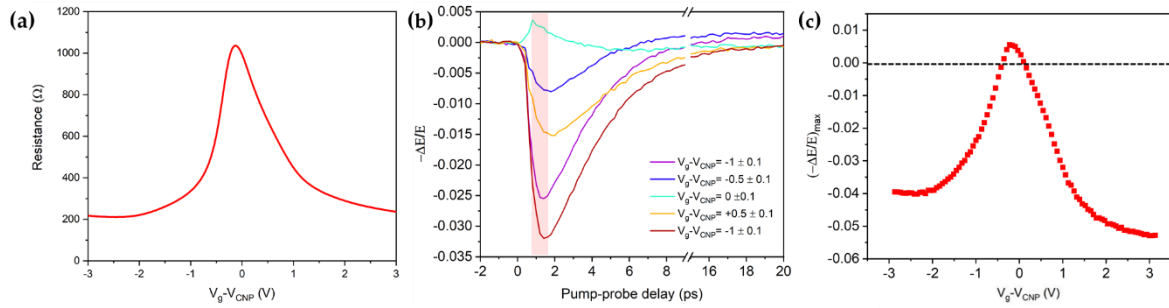


Figure S2: (a) Resistance of graphene in heterostructure at different gate voltages, (b) OPTP dynamics of WS₂/Gr heterostructure following 800 nm photoexcitation at different gate voltages, (c) maximum photoconductivity at ~1.4 ps as a function of gate voltages (for sample B).

Section 2: Theoretical calculation

The hot carrier densities are calculated using the following equations [14], [23].

The hot electron density is:

$$n_{HE} = \int_{E_F}^{\infty} v(E) f_e(E) dE \quad (3.3)$$

where the $v(E) = \frac{2E}{\pi(\hbar v_F)^2}$ is the density of state (\hbar is reduced Planck constant and v_F is Fermi velocity) and the Fermi-Dirac distribution for electrons is expressed as:

$$f_e(E) = \frac{1}{e^{(E-E_F)/k_B T} + 1}$$

where k_B is the Boltzmann constant and T is the temperature.

Similarly, the hot hole density is:

$$n_{HH} = \int_{-E_F}^{\infty} v(E) f_h(E) dE \quad (3.4)$$

The Fermi-Dirac distribution for holes is:

$$f_h(E) = \frac{1}{e^{(E+E_F)/k_B T} + 1}$$

The photo-thermionic emission relies on the carrier temperature and only the electrons which have sufficient energy can overcome the barrier and be injected into WS₂ [9]. The hot electron density above the energy barrier that can be transferred is calculated using the following equation:

$$n_{CTE} = \int_{E_{electron\ barrier}}^{\infty} v(E) f_e(E) dE \quad (3.5)$$

The hot hole density above the energy barrier that can be transferred is:

$$n_{CTH} = \int_{E_{hole\ barrier}}^{\infty} v(E) f_h(E) dE \quad (3.6)$$

The charge transferred (CT) carrier density is:

$$n_{CT} = n_{CTE} - n_{CTH} \quad (3.7)$$

The efficiency of the charge transfer can be calculated by:

$$n_{CT} = \eta_{CTE} - \eta_{CTH} = \frac{n_{CT}}{n_{HE}} - \frac{n_{CTH}}{n_{HH}} \quad (3.8)$$

The high electronic temperature leads to the redistribution of electrons and hole in conduction and valence band, shifting the effective Fermi energy level (quasi-equilibrium) according to this equation [24]:

$$\Delta|E_F| \approx -\frac{\pi^2}{6} \left(\frac{K_B T_e}{E_2} \right)^2 \quad (3.9)$$

where T_e is electron temperature. The photoconductivity $\Delta\sigma$ (or ΔN) also is related to electronic temperature via equation (3.11):

$$\left(\frac{-\Delta E}{E} \right) \sim \Delta\sigma \sim e \cdot \Delta N \cdot \Delta\mu \sim e(N' \cdot \mu' - N \cdot \mu) \quad (3.10)$$

where N, μ and N', μ' are the carrier density and charge mobility before and after photoexcitation, respectively.

$$\left(\frac{-\Delta E}{E} \right) \sim \Delta\sigma = \alpha T_e(F, E_F) \quad (3.11)$$

In the case of, $|E_F| \geq 0.1$ eV,

$$T_e = \alpha(T_L^3 + \frac{3\gamma F}{\alpha})^{1/2} \quad (3.12)$$

where T_L is lattice temperature,

$$\alpha = \frac{2\pi}{3} \frac{K_B^2 E_F}{(\hbar v_F)^2}$$

However, for $|E_F| \leq 0.1$ eV

$$T_e = \alpha(T_L^3 + \frac{3\gamma F}{\beta})^{1/3} \quad (3.13)$$

where

$$\beta = \frac{18 \times \zeta(3) \times K_B^2}{(\pi \hbar v_F)^2}$$

$$\zeta(3) = 1.202$$

$\gamma = 2.3\%$ as the absorption of graphene at 1.55eV is 2.3%.

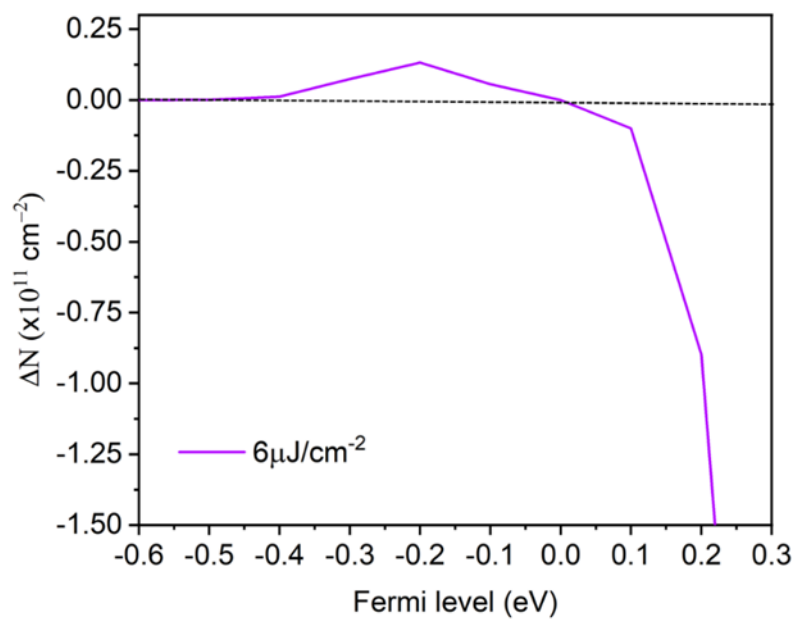


Figure S3: The calculated relative ratio of carrier density above the energy barrier following photoexcitation and heating at different graphene Fermi levels.

References

- [1] Y. Liu et al., "Van der Waals integration before and beyond two-dimensional materials", *Nature*, vol. 567, pp 323–333, 2019.
- [2] D. Jariwala et al., "Mixed-dimensional van der Waals heterostructures", *Nature Materials*, vol.16, pp 170-181, 2017.
- [3] K. S. Novoselov et al., "2D materials and van der Waals heterostructures", *Science*, vol. 353, aac9439, 2016.
- [4] A. K. Geim et al., "Van der Waals heterostructures", *Nature*, vol. 499, pp. 419-425, 2013.
- [5] J. J. Shim et al., "Recent progress in Van der Waals (vdW) heterojunction-based electronic and optoelectronic devices", *Carbon*, vol. 133, pp. 78-89, 2018.
- [6] M. Massicotte et al., "Picosecond photoresponse in van der Waals heterostructures", *Nature Nanotechnology*, vol. 11, pp. 42-46, 2016.
- [7] F. H. L. Koppens et al., "Photodetectors based on graphene, other two-dimensional materials, and hybrid systems", *Nature Nanotechnology*, vol. 9, pp. 780-793, 2014.
- [8] G. Konstantatos et al., "Current status and technological prospect of photodetectors based on two-dimensional materials", *Nature Communication.*, vol. 9, pp. 9-11, 2018.
- [9] S. Fu et al., "Long-lived charge separation following pump-energy dependent ultrafast charge transfer in graphene/WS₂ heterostructures", *arXiv: 2007.08932*, 2020.
- [10] Y. Chen et al., "Highly efficient hot electron harvesting from graphene before electron-hole thermalization", *Science Advances*, vol.5, pp. 1-8, 2019.
- [11] A. K. Geim et al. "The rise of graphene", *Nature Materials*, vol. 6, pp. 183-191, 2007.
- [12] K. I. Bolotin et al., "Ultrahigh electron mobility in suspended graphene", *Solid State Communications*, vol. 146, pp. 351-355, 2008.
- [13] C. R. Dean et al., "Boron nitride substrates for high-quality graphene electronics", *Nature Nanotechnology*, vol. 5, pp. 722-726, 2010.
- [14] A. J. Frenzel et al., "Semiconducting-to-metallic photoconductivity crossover and temperature-dependent Drude weight in graphene", *Physical Review Letters*, vol. 113, 056602, 2014.
- [15] J. Horng et al., "Drude conductivity of Dirac fermions in graphene", *Physical Review B*, vol. 83, 165113, 2011.
- [16] L. Ren et al., "Terahertz and infrared spectroscopy of gated large-area graphene", *Nano Letters*, vol. 12, pp. 3711-3715, 2012.
- [17] S. A. Jensen et al., "Competing ultrafast energy relaxation pathways in photoexcited graphene", *Nano Letters*, vol. 14, pp. 5839-5845, 2014.

- [18] Y. M. Lin et al., "Operation of graphene transistors at gigahertz frequencies", *Nano Letters*, vol. 9, pp. 422-426, 2009.
- [19] T. Low et al., "Graphene plasmonics for terahertz to mid-infrared applications", *ACS Nano*, vol. 8, pp. 1086-1101, 2014.
- [20] S. Vaziri et al., "A graphene-based hot-electron transistor", *Nano Letters*, vol. 13, pp. 1435-1439, 2013.
- [21] N. M. Gabor et al., "Hot carrier-assisted intrinsic photoresponse in graphene", *Science*, vol. 334, pp. 648-652, 2011.
- [22] C. H. Lui, et al., "Ultrafast photoluminescence from graphene", *Physical Review Letter.*, vol. 105, 27404, 2010.
- [23] S. F. Shi et al., "Controlling graphene ultrafast hot carrier response from metal-like to semiconductor-like by electrostatic gating", *Nano Letters*, vol. 14, pp. 1578-1582, 2014.
- [24] G. Jnawali, et al., "Observation of a transient decrease in terahertz conductivity of single-layer graphene induced by ultrafast optical excitation", *Nano Letters*, vol. 13, pp. 524-530, 2013.
- [25] A. J. Frenzel et al., "Observation of suppressed terahertz absorption in photoexcited graphene", *Applied Physics Letters*, vol. 102, 113111, 2013.
- [26] K. J. Tielrooij et al., "Photoexcitation cascade and multiple hot-carrier generation in graphene", *Nature Physics*, vol. 9, pp. 248-252, 2013.
- [27] J. H. Strait et al., "Very slow cooling dynamics of photoexcited carriers in graphene observed by optical-pump terahertz-probe spectroscopy", *Nano Letters*, vol. 11, pp. 4902-4906, 2011.
- [28] P. A. George, Ultrafast optical-pump Terahertz-probe spectroscopy of the carrier relaxation and recombination dynamics in epitaxial graphene", *Nano Letters*, vol. 8, pp. 17-20, 2008.
- [29] C. J. Docherty et al., "Extreme sensitivity of graphene photoconductivity to environmental gases", *Nature Communications*, vol. 3, 1228, 2012.
- [30] X. Li et al., "Large-area synthesis of high-quality and uniform graphene films on copper foils", *Science*, vol. 324, pp. 1312-1314, 2009.
- [31] I. Gierz et al., "Snapshots of non-equilibrium Dirac carrier distributions in graphene", *Nature Materials*, vol. 12, pp. 1119-1124, 2013.
- [32] R. Schmidt et al., "Ultrafast coulomb-induced intervalley coupling in atomically thin WS₂", *Nano Letters*, vol. 16, pp. 2945-2950, 2016.
- [33] M. Müller et al., "Temperature dependence of the conductivity of ballistic graphene", *Physical Review Letters*, vol. 103, 196801, 2009.
- [34] T. Li et al., "Femtosecond population inversion and stimulated emission of dense Dirac fermions in graphene", *Physical Review Letters*, vol. 108, pp. 1-5, 2012.
- [35] M. W. Graham et al., "Photocurrent measurements of supercollision cooling in graphene", *Nature Physics*, vol. 9, pp. 103-108, 2013.

- [36] K. M. Dani et al., "Intraband conductivity response in graphene observed using ultrafast infrared-pump visible-probe spectroscopy", *Physical Review B*, vol. 86, 125403, 2012.
- [37] T. Plötzing, et al., "Experimental verification of carrier multiplication in graphene", *Nano Letters*, vol. 14, pp. 5371-5375, 2014.
- [38] F. Wendler et al., "Carrier multiplication in graphene under Landau quantization", *Nature Communications*, vol. 5, 3703, 2014.
- [39] D. Brida et al., "Ultrafast collinear scattering and carrier multiplication in graphene", *Nature Communications*, vol. 4, 1987, 2013.
- [40] J. C. W. Song et al., "Photoexcited carrier dynamics and impact-excitation cascade in graphene", *Physical Review Letters*, vol. 87, 155429, 2013.
- [41] J. C. Johannsen et al., "Direct view of hot carrier dynamics in graphene", *Physical Review Letters*, vol. 111, 027403, 2013.
- [42] K. J. Tielrooij et al., "Photoexcitation cascade and multiple hot-carrier generation in graphene", *Nature Physics*, vol. 9, pp. 248-252, 2013.
- [43] S. Aeschlimann et al., "Direct evidence for efficient ultrafast charge separation in epitaxial WS₂ / graphene heterostructure", *Science Advances*, eaay0761, 2016.
- [44] M. Massicotte et al., "Photo-thermionic effect in vertical graphene heterostructures", *Nature Communications*, vol. 7, 12174, 2016.
- [45] W. J. Yu et al., "Highly efficient gate-tunable photocurrent generation in vertical heterostructures of layered materials", *Nature Nanotechnology*, vol. 8, pp. 952-958, 2013.
- [46] L. Yuan et al., "Photocarrier generation from interlayer charge-transfer transitions in WS₂ -graphene heterostructures", *Science Advances*, 1700324, 2018.
- [47] M. T. Mihnev et al., "Microscopic origins of the terahertz carrier relaxation and cooling dynamics in graphene", *Nature Communications*, vol. 7, 11617, 2016.
- [48] K. J. Tielrooij et al., "Generation of photovoltage in graphene on a femtosecond timescale through efficient carrier heating", *Nature Nanotechnology*, vol. 10, pp. 437-443, 2015.
- [49] A. Raja et al., "Coulomb engineering of the bandgap and excitons in two-dimensional materials", *Nature Communications*, vol. 8, 15251, 2017.
- [50] B. Schuler et al., "Large spin-orbit splitting of deep in-gap defect states of engineered Sulfur vacancies in Monolayer WS₂", *Physical Review Letters*, vol. 123, 76801, 2019.
- [51] J. Pijpers, *Carrier dynamics in photovoltaic nanostructures*, Amsterdam University, 2010.
- [52] R. Ulbricht, *"Charge carriers in semiconductors: Loose, confined, trapped"*, Amsterdam University, 2012.
- [53] S. A. Jensen, *Charge carrier dynamics in photovoltaic materials*, Amsterdam University, 2014.

- [54] A. Paulke, "Transient conductivity measurements using Terahertz time-domain spectroscopy", University of Potsdam, 2013.
- [55] M. Zoltan et al., "Thermodynamic picture of ultrafast charge transport in graphene", *Nature Communications*, vol. 6, 7655, 2015.
- [56] L. Kunneman et al., "Nature and decay pathways of photoexcited states in CdSe and CdSe/CdS nanoplatelets", *Nano Letters*, vol.14, pp. 7039-7045, 2011.
- [57] I. Ivanov, "Terahertz spectroscopy of graphene and graphene nanostructures" University of Mainz, 2018.
- [58] E. Del Corro et al., "Atypical exciton-phonon interactions in WS₂ and WSe₂ monolayers revealed by resonance Raman spectroscopy", *Nano Letters*, vol. 16, pp. 2363-2368, 2016.
- [59] J. Yan et al., "Electric field effect tuning of electron-phonon coupling in graphene", *Physical Review Letters*, vol. 98, 166802, 2007.
- [60] G. Burwell et al., "Investigation of the utility of cellulose acetate butyrate in minimal residue graphene transfer, lithography, and plasma treatments", *Microelectronic Engineering*, vol. 146, pp. 81-84, 2015.
- [61] Y. Yu et al., "Gate-tunable phase transitions in thin flakes of 1T-TaS₂", *Nature Nanotechnology*, vol. 10, pp 270-276, 2015.